

# Recent Precipitation Decrease Across the Western Greenland Ice Sheet Percolation Zone

Lewis, Gabriel<sup>1</sup>; Osterberg, Erich<sup>1</sup>; Hawley, Robert<sup>1</sup>; Marshall, Hans Peter<sup>2</sup>; Meehan, Tate<sup>2</sup>; Graeter, Karina<sup>3</sup>; McCarthy, Forrest<sup>4</sup>; Overly, Thomas<sup>5,6</sup>; Thundercloud, Zayta<sup>1</sup>; Ferris, David<sup>1</sup>

<sup>1</sup>Department of Earth Sciences, Dartmouth College, Hanover, NH, USA

<sup>2</sup>Geosciences Department, Boise State University, Boise, ID, USA

<sup>3</sup>Office of Sustainability, University of Maine, Orono, ME, USA

<sup>4</sup>College of Fisheries and Ocean Sciences, University of Alaska Fairbanks, Fairbanks, AK, USA

<sup>5</sup>NASA Cryospheric Sciences Laboratory, NASA Goddard Space Flight Center, Greenbelt, MD, USA

<sup>6</sup>Earth System Science Interdisciplinary Center (ESSIC), University of Maryland, College Park, MD, USA

Correspondence to: Gabriel Lewis (Gabriel.M.Lewis.GR@dartmouth.edu)

## Abstract

The mass balance of the Greenland Ice Sheet (GrIS) in a warming climate is of critical interest in the context of future sea-level rise. Increased melting in the GrIS percolation zone due to atmospheric warming over the past several decades has led to increased mass loss at lower elevations. Previous studies have hypothesized that this warming is accompanied by a precipitation increase, as would be expected from the Clausius-Clapeyron relationship, compensating for some of the melt-induced mass loss throughout the Western GrIS. This study tests that hypothesis by calculating snow accumulation rates and trends across the Western GrIS percolation zone, providing new critical accumulation rate estimates in regions with sparse *in situ* data or data that does not span the recent accelerating surface melt. We present accumulation records from sixteen 22 – 32 m long firn cores and 4436 km of ground penetrating-radar, covering the past 20 – 60 years of accumulation, collected across the Western GrIS percolation zone as part of the Greenland Traverse for Accumulation and Climate Studies (GreenTrACS) project. Trends from both radar and firn cores, as well as commonly used regional climate models, show decreasing accumulation rates and precipitation of  $2.4 \pm 1.5$  %  $a^{-1}$  over the 1996 – 2016 period, which we attribute to shifting storm-tracks related to stronger atmospheric summer blocking over Greenland. Changes in atmospheric circulation over the past 20 years, specifically anomalously high summertime blocking, have reduced GrIS surface mass balance through both an increase in surface melting and a decrease in accumulation rates.

## 1. Introduction

Greenland Ice Sheet (GrIS) mass loss has accelerated over the past few decades, with modern mass loss rates more than double those from Antarctica (van den Broeke et al., 2016). The 2010-2018 GrIS mass loss was calculated as  $286 \pm 20$  Gt  $a^{-1}$  (Mouginot et al., 2019), contributing  $0.7 \pm 0.2$  mm  $a^{-1}$  of sea level rise. Over the past 20 years, the largest warming rates (Hanna et al., 2012) and fastest mass loss have occurred in Western

34 Greenland ( $26 \pm 7$  GT a<sup>-2</sup> in basins F + G of Sasgen et al., 2012). Here, regional scale models calculate a  
35 surface mass balance (SMB) decrease ranging from 31.1% (European Centre for Medium Range Weather  
36 Forecasting downscaled; ECMWFd) to 76.5% (Modèle Atmosphérique Régional; MAR) over the 1996 –  
37 2008 period (Vernon et al., 2013) as a result of higher surface melt and runoff (van den Broeke et al., 2009,  
38 2016). Modern surface melt rates are at their highest levels of at least the last 450 years across Western  
39 Greenland (Graeter et al., 2018) and more broadly throughout Greenland (Trusel et al., 2018). In particular,  
40 ice core records from Western Greenland show an abrupt increase in surface melt rates beginning in the  
41 middle-late 1990's due to a combination of higher North Atlantic sea surface temperatures, enhanced  
42 summertime blocking highs, and anthropogenic warming (Graeter et al., 2018).

43  
44 Enhanced GrIS surface melt is driven fundamentally by rising Greenland summer temperature trends  
45 upwards of  $0.135 \pm 0.047$  °C a<sup>-1</sup> from 1982 – 2011 (Hall et al., 2013; Reeves Eyre and Zeng, 2017). Basic  
46 physics implies that rising temperatures should cause an increase in accumulation rates over the ice sheet due  
47 to the Clausius-Clapeyron relationship – warmer air has a higher saturation vapor pressure, potentially  
48 leading to more precipitation (Box et al., 2006; Buchardt et al., 2012). The Coupled Model Intercomparison  
49 Project, phase 5 (CMIP5) predicts precipitation increases of 20 – 50% over the GrIS by the end of the 21<sup>st</sup>  
50 century (Bintanja and Selten, 2014), partially offsetting mass loss and sea-level rise from enhanced summer  
51 melt and runoff. However, most *in situ* records of Greenland snow accumulation do not span the modern  
52 period of rapid warming since the mid-1990s, making it difficult to determine whether accumulation rates  
53 have been increasing with warming temperatures as predicted. For example, the Program for Arctic Regional  
54 Climate Assessment (PARCA) campaign collected accumulation rate data from a network of 49 ice and firn  
55 cores in 1997-1998 (Mosley-Thompson et al., 2001), just at the onset of accelerated surface melting (Graeter  
56 et al., 2018). There have been no published *in situ* accumulation records from the Western GrIS percolation  
57 zone for the past decade. Updated *in situ* snow accumulation rates are needed from this region to assess recent  
58 changes in accumulation rates during this period of warming and SMB loss from melt and runoff.

59  
60 In addition to measuring snow accumulation rates with ice cores and automated snow depth sensors, several  
61 studies have used ground-based and airborne radar to calculate GrIS accumulation rates and trends (e.g.  
62 Medley et al., 2013; Spikes et al., 2004; Hawley et al., 2014; Koenig et al., 2016). We build upon these  
63 previous studies by collecting GPR data across the lower percolation zone of Western Greenland, where  
64 airborne radargrams are often obscured by refrozen melt percolation (Nghiem et al., 2005). The *in situ* GPR  
65 used in this study operates using a UHF pulsed radar, while other systems such as frequency modulated  
66 continuous wave (FMCW) radars use phase-sensitive antennas that include both amplitude and phase

67 information. By having our GPR antenna coupled with the snow, we avoid losing energy, and, therefore,  
68 penetration depth, from a strong reflection off of the snow-air interface.

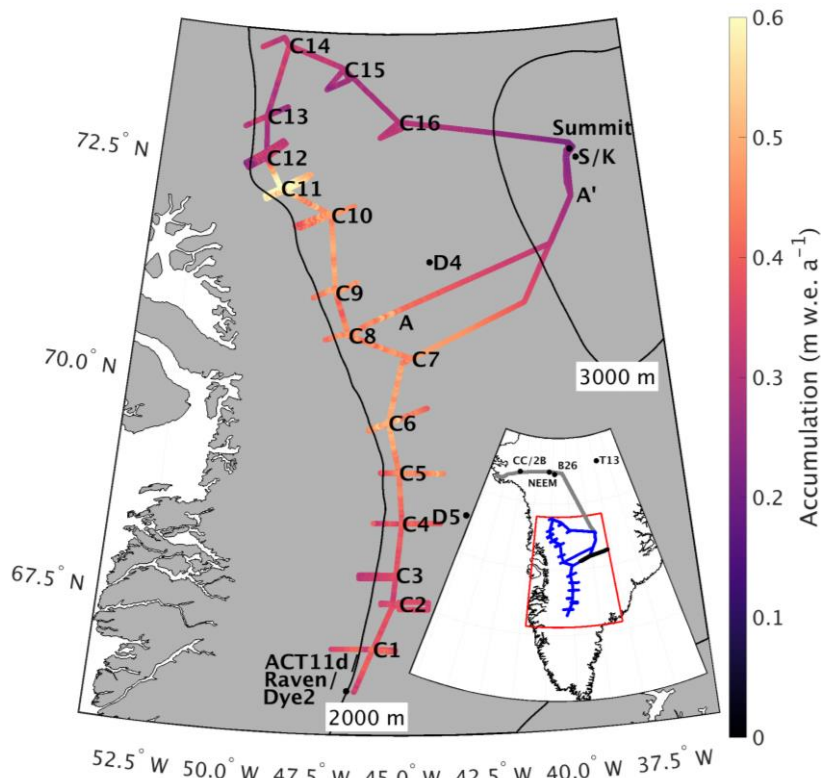
69

70 In addition to temperature-precipitation relationships through the Clausius-Clapeyron relationship, previous  
71 studies have analyzed the dynamic climate controls on Greenland precipitation. Mernild et al. (2014), Auger  
72 et al. (2017), and Lewis et al. (2017) have hypothesized that a positive Atlantic Multidecadal Oscillation  
73 (AMO) index correlates with rising accumulation rates over most of the GrIS interior, since higher sea surface  
74 temperatures increase moisture flux over the GrIS and induce greater snowfall. In addition, high pressure  
75 (blocking) systems east of Greenland tend to deflect eastward-moving storms over central Greenland and  
76 increase precipitation, whereas blocking directly over Greenland or in Baffin Bay has the potential to  
77 decrease accumulation rates over the GrIS by displacing the polar jet stream and corresponding storm tracks  
78 equatorward (Auger et al., 2017). Over the 1991 – 2015 period there has been particularly strong summertime  
79 Greenland blocking (Hanna et al., 2016), but its effects on GrIS accumulation rates have not been determined  
80 with *in situ* data.

81

82 Here we develop new accumulation records across the Western GrIS percolation zone using sixteen firn cores  
83 and 4436 km of GPR data collected during an over-ice traverse spanning two field seasons. We evaluate the  
84 veracity of the accumulation data through comparisons of our firn core time series with previous  
85 measurements. We quantify multi-year trends in accumulation rates across Western Greenland to test the  
86 hypothesis that precipitation has recently increased from the Clausius-Clapeyron relationship and higher GrIS  
87 temperatures. Further, we assess the ability of RCMs to capture the year-to-year variability and multi-year  
88 trends in Western GrIS accumulation rates. Finally, we evaluate relationships between recent accumulation  
89 rate trends and atmospheric circulation patterns, particularly changes in storm tracks.

90



91

92

93

94

95

**Figure 1. Average accumulation rates across the GreenTrACS traverse for the length of each record showing the location of each firn core, ACT11d, D4, D5, Katie (K), Raven/Dye-2, and Sandy (S) ice cores, and Summit Station. Transect A-A' discussed in Section 3.3. Inset shows locations of Camp Century (CC), 2Barrel (2B), NEEM, B26, and TUNU2013 (T13) ice cores, as well as locations of EGIG (black), GrIT (grey), and GreenTrACS (blue) traverses.**

96

## 2. Methods

97

98

99

100

101

102

103

104

105

106

107

108

This study uses data from the 2016 – 2017 Greenland Traverse for Accumulation and Climate Studies (GreenTrACS), which measured accumulation rates and melt across the Western GrIS percolation zone over two summer snowmobile traverses (closely following the 2150 m a.s.l. elevation contour). The May – June 2016 season traversed 860 km from Raven/Dye-2 northward to Summit Station, while the May – June 2017 traverse made a 1230 km clockwise loop starting and ending at Summit Station (Figure 1). This manuscript focuses on accumulation rates derived from 400 MHz GPR data collected along the entire traverse path, as well as sixteen shallow (22 – 32 m deep) firn cores spaced 40 – 100 km apart along the backbone of the traverse (Figure 1). Firn Cores 1 – 7 were collected in 2016 and Cores 8 – 16 were collected in 2017. We returned to the Core 7 location at the beginning of the 2017 traverse to recover a weather station and to connect the two season’s GPR data. Additionally, we collected GPR data ~30 – 70 km east and west of each core site, hereafter called “spurs”, to measure changes in accumulation rates along strong elevation gradients (see Figure 1).

## 2.1. GPS Positioning

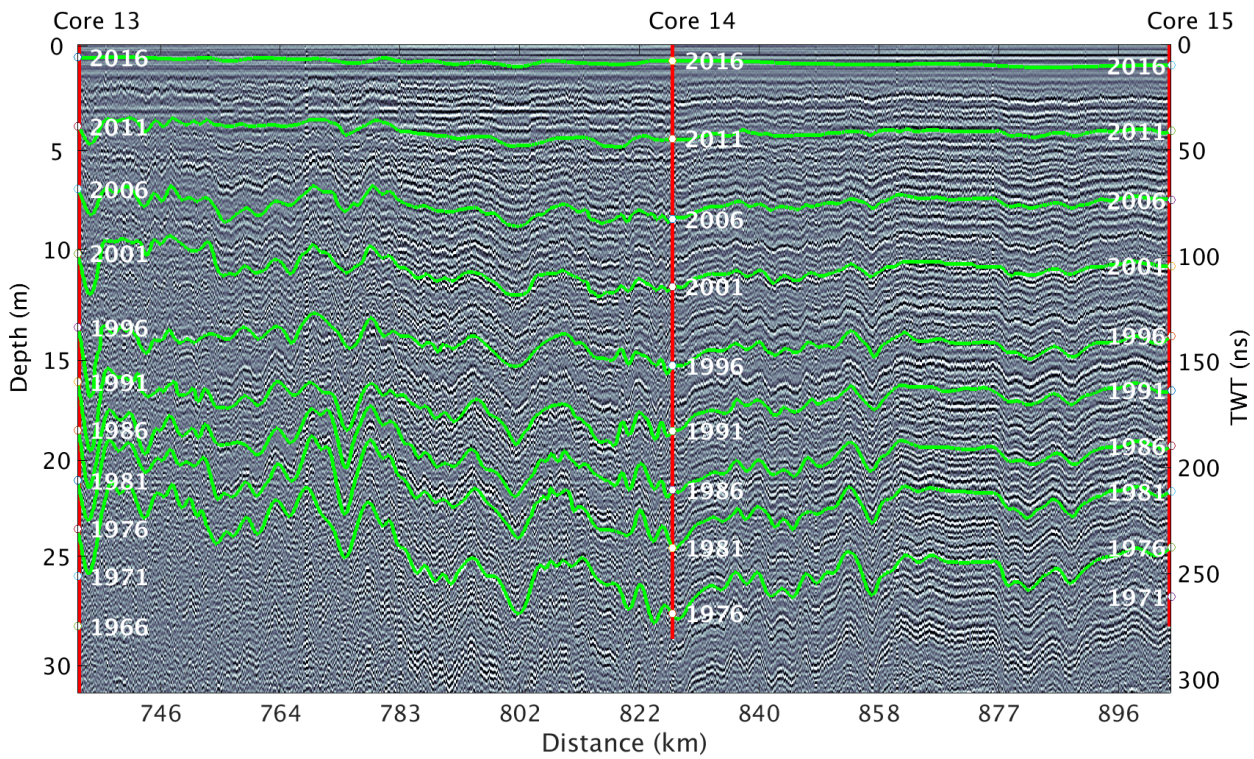
During the 2016 traverse we collected GPS data using a Trimble NetR8 reference receiver with a Zephyr Geodetic antenna mounted to a Nansen sled ~5 m in front of the GPR antenna. For each spur and the tail ends of each transect between core sites we performed differential corrections to the GPS data using RTKLIB 2.4.1 and a Trimble NetR8 base station near the core site. Between spurs, when not operating a base station, we post-processed GPS data in precise point positioning mode (Zumberge et al., 1997). Estimated root-mean-square horizontal errors were generally between 13 and 18 cm from standard deviations calculated during stationary periods at the end of spurs. To co-register GPR and GPS data, we used time stamps embedded in the two data streams and locations where we stopped to save GPR files, approximately every 15 km. The time drift in the GPR logger is negligible over these durations.

During the 2017 traverse we used GPS data from a Garmin 19x GPS receiver wired directly to the GPR instrument, which recorded position data at every radar sample with RMS values of 3 m. During radar processing we average 75 adjacent traces, corresponding to a distance of ~20 m, so errors in GPS positioning have a negligible effect on the final dataset.

## 2.2. Ground-penetrating radar

We develop a spatially continuous record of accumulation rates using GPR profiles collected with Geophysical Survey Systems Inc. (GSSI) SIR-3000 (during 2016) and SIR-30 (during 2017) radar units with a 400 MHz antenna (following Hawley et al., 2014). The antenna was towed on the snow surface in a small plastic sled ~5 m behind a wooden Nansen sled and ~15 m behind a snow machine. We recorded 2048 samples (2016) and 4096 samples (2017) per trace over a range window of 800 ns (Figure 2). The 400 MHz short-pulse radar has a range resolution (ability to resolve distinct features) of  $0.35 \pm 0.10$  m in firn, which is fine enough to resolve Internal Reflecting Horizons (IRHs) that have been shown to represent isochrones (Medley et al., 2013; Rodriguez-Morales et al., 2014; Spikes et al., 2004; Hawley et al., 2014). We recorded 10 traces per second, which at the snowmobile's average travel speed of approximately  $2.75 \text{ m s}^{-1}$  results in ~3.6 traces recorded per meter. Note that this spacing between traces varies with vehicle speed.





136  
137  
138  
139  
140

**Figure 2. Radargram showing the top 32 m of the transect along the main 2017 traverse from Core 13 to Core 15. Cores are indicated as red lines down to their final depth, with dates plotted every 5 years at corresponding depths. Traced internal reflecting horizons are shown as isochronous green lines. The depth scale on the vertical axis is calculated from the TWT-depth conversion (see Section 2.4) for Core 13, although there is no visual difference in depth scale across this radargram.**

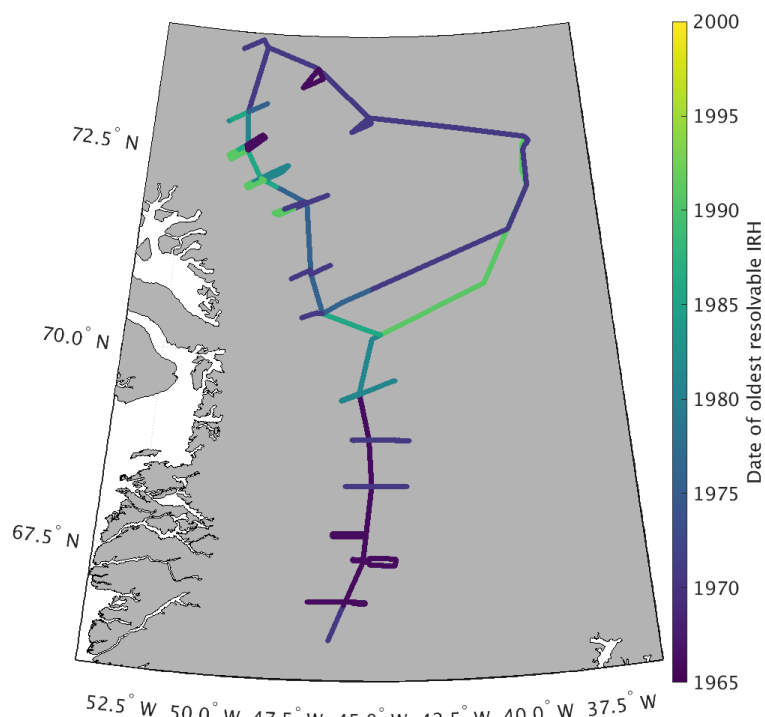
141 Depending on signal attenuation within the firn column, IRHs can be traced to a depth of 20 – 50 m (Figure  
142 2), providing accumulation records over the past 20 – 60 years (Figure 3). For areas with high attenuation  
143 (i.e. shallow penetration of the radar signal), such as lower elevation regions with more refrozen melt layers,  
144 we calculate accumulation results for shorter time periods. We are not able to trace as many IRHs to the west  
145 of Cores 10 – 13 compared to the east due to higher signal attenuation, resulting in slightly different (less  
146 than  $0.03 \text{ m w.e a}^{-1}$ ) average accumulation values on either side of these core locations (Figure 3). Likewise,  
147 we experienced an equipment malfunction at the end of the 2016 traverse, reducing the number of observable  
148 IRHs from Core 7 to Summit Station (Figure 3). We have less confidence in calculated accumulation rates  
149 throughout this section of the traverse due to this malfunction, although the 2017 Summit to Core 8 interval  
150 overlaps nicely with the last 140 km of the problematic 2016 interval, and provides high quality accumulation  
151 measurements for this section near Summit Station.

152

153 We reduce the GPR data volume and signal noise by averaging 75 adjacent traces, which has the effect of  
154 suppressing random noise by the principle of trace stacking (Yilmaz, 2001). We apply a combination of  
155 median trace filtering, residual mean filtering (Gerlitz et al., 1993), and bandpass filtering using a butterworth  
156 design (Selesnick and Sidney Burrus, 1998) between 200 – 800 MHz. For data visualization, we apply an  
157 automatic gain control (Yilmaz, 2001) to give the interpreter more confidence when picking IRHs.

158

159



160

161

162

**Figure 3: Date of oldest resolvable internal reflecting horizon throughout the entire GreenTrACS traverse route. Anomalously young ages from Core 7 to Summit are due to equipment malfunction.**

163

164

### 2.3. Firn core processing and density profiles

165

166

167

168

169

170

171

172

173

174

175

176

The amount of snow mass and the time span between IRHs are necessary to calculate accumulation rates from the GPR profiles. The accumulation rate is a function of the depth-age scale, travel time-depth conversion rate, and the firn density profile. We obtain the depth-age and depth-density scales from each of the shallow firn cores collected along the GreenTrACS traverse, and from density models based on temperature and accumulation rate data.

The sixteen firn cores were drilled using an Ice Drilling Program hand auger with a Kyne sidewinder attachment (see Graeter et al., 2018). We sampled the firn cores for chemical measurements using a continuous ice core melter system with discrete sampling (Osterberg et al., 2006). We used an Abakus (Klotz) laser particle detector to measure microparticle concentrations and size distribution from the continuous ice core meltwater stream, a Dionex Model ICS5000 capillary ion chromatograph to measure major ion ( $\text{Na}^+$ ,  $\text{Mg}^{2+}$ ,  $\text{Ca}^{2+}$ ,  $\text{K}^+$ ,  $\text{NH}_4^+$ ,  $\text{Cl}^-$ ,  $\text{NO}_3^-$ ,  $\text{SO}_4^{2-}$ ) and methanesulfonic acid concentrations, and a Picarro L1102-I and

177 a Los Gatos Research Liquid Water Isotope Analyzer to measure oxygen and hydrogen isotope ratios ( $\delta^{18}\text{O}$ ,  
178  $\delta\text{D}$ ; Graeter et al., 2018).

179  
202 We determine depth-age curves for each core by identifying annual layers based on seasonal oscillations in  
203  $\delta^{18}\text{O}$  and the concentrations of major ions and dust, consistent with previous ice core studies in this region  
204 (Graeter et al., 2018; Mosley-Thompson et al., 2001; Osterberg et al., 2015). While meltwater percolation  
205 smooths the signal of some of these tracers, we can still confidently determine the depth-age curve using  
206 nearly unperturbed oscillations in  $\delta^{18}\text{O}$  and dust. We combine the depth-age scales with measured density to  
207 calculate annual accumulation rates at the firn core sites.

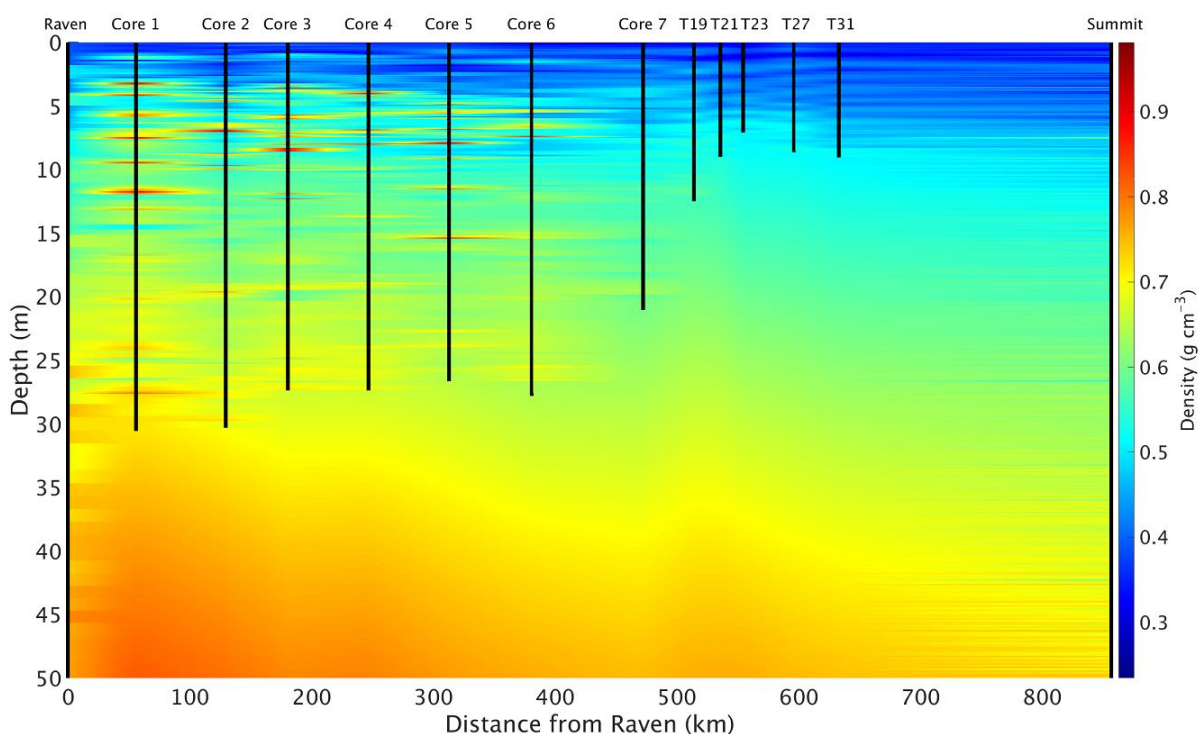
208  
209 At each firn core and at the ends of each spur, we measured the density in the top meter of snow using a 1000  
210  $\text{cm}^3$  SnowMetrics cutter. To calculate density profiles from the firn cores, we measured the mass, length, and  
211 diameter of 0.03–1 m long core segments in the field and again after transporting the cores to the Dartmouth  
212 College Ice Core Laboratory. Additionally, we measured melt layer thickness in the laboratory following  
213 Graeter et al. (2018). To calculate accumulation rates at Raven/Dye-2, we use density data from a 119.6 m  
214 long firn core collected in 1997 (Bales et al., 2009) and a 19.3 m long core collected from the same location  
215 in 2015, which did not include accumulation rate data (Vandecrux et al., 2018). For this location we use the  
216 most recent density data for the near-surface and the older densities for depths below the 2015 core. Likewise,  
217 we use a density profile from a 109 m long firn core collected from Summit in 2010 (Mary Albert, personal  
218 communication, 2015). We also incorporate density data from measurements along the EGIG traverse at T19,  
219 T21, T23, T27, and T31 to improve the density profile between Core 7 and Summit (Morris and Wingham,  
220 2014).

221  
222 After collecting each firn core, we measured borehole temperature for 24 – 48 hours using a 20 m long  
223 thermistor string. We estimate mean annual temperature from the deepest thermistor on the twenty-  
224 thermistor-string. These measurements agree with MODIS satellite derived mean annual temperature (Hall  
225 et al., 2012) to within  $\pm 1$  °C for each firn core location. For the location of each firn core, we use the depth-  
226 density data from that core and calculate a Herron and Langway (1980) depth-density model for depths below  
227 the core using our measured mean annual temperature, firn core mean annual accumulation rates, and top-  
228 meter snow density. Likewise, we calculate Herron-Langway profiles for the ends of each spur using MODIS  
229 satellite derived mean annual temperature (Hall et al., 2012), MAR modeled accumulation rates (Burgess et  
230 al., 2010), and the measured snow density in the upper meter of each of the spur’s snow pits. Finally, we  
231 interpolate depth-density profiles both between firn cores and along radar spurs to estimate the depth-density



232 matrix everywhere along our traverse (Figure 4). Final calculated accumulation rates are insensitive to the  
233 input accumulation parameter we use to calculate our Herron-Langway models (Lewis et al., 2017).

234  
235 As shown in Figure 4, ice layers within several firn cores are extrapolated laterally along the traverse,  
236 although these dense lenses are typically both localized and heterogeneous at these elevations (Brown et al.,  
237 2011; Rennermalm et al., 2013). Numerous studies have documented the heterogeneity of firn throughout  
238 the percolation zone and the complications of calculating SMB due to ice pipes and lenses (Brown et al.,  
239 2011, 2012; De La Peña et al., 2015). Here we attempt to accurately calculate accumulation rates using  
240 interpolated firn cores and *in situ* GPR throughout this complicated region. Our ice lens density interpolation  
241 is as accurate as possible between firn cores without additional *in situ* data, and this estimation does not  
242 significantly alter our results, as discussed in Section 2.6, since the ice layers represent a small fraction of the  
243 total depth to IRHs.



244  
245 **Figure 4. Depth-density profile along the main 2016 traverse used for calculation of electromagnetic wave velocity and accumulation**  
246 **rates in this study. Densities are linearly interpolated between the two nearest cores and are modeled using Herron-Langway profiles**  
247 **below the depth of each core. The left and right boundary data come from the Raven/Dye-2 and Summit firn cores, respectively. Ice**  
248 **layers in Cores 1 – 5 are clearly visible as red lenses, but their extent is, in reality, likely more localized.**

## 249 250 **2.4. Travel-time to depth conversion**

251 We convert the radar travel time to depth by iteratively multiplying the velocity of the electromagnetic wave  
252 by the signal’s one-way travel time to each IRH. The electromagnetic speed of the radar wave,  $v$  ( $\text{m s}^{-1}$ ), is

253 calculated from the relative dielectric permittivity,  $\epsilon_r$  (dimensionless), and the speed of light in a vacuum,  $c$   
254 ( $3 \times 10^8 \text{ m s}^{-1}$ ), from

$$255 \quad v = \frac{c}{\sqrt{\epsilon_r}} \quad (1).$$

256 In turn, we calculate the relative dielectric permittivity from the density,  $\rho$  ( $\text{g cm}^{-3}$ ), of snow and ice at depth,  
257 as shown in Figure 4, for each radar trace at every range bin (following Kovacs et al., 1995) by

$$258 \quad \epsilon_r = (1.0 + 0.845 * \rho)^2 \quad (2).$$

259 We calculate the depth of each subsequent radar sample for each trace in the profile using the radar travel  
260 time and velocity profile from equations 1 and 2, following Hawley et al. (2014) and Lewis et al. (2017).

261

## 262 **2.5. Internal reflecting horizons**

263 We manually select 10 clear, strong IRHs spaced approximately 5 years apart to consistently trace from  
264 Raven/Dye-2 to Summit Station and throughout the 2017 main traverse (Figure 2). We trace each layer  
265 manually by visually identifying strong amplitude peaks throughout the radargram, starting with the 2016  
266 layer and working downwards. We use a spline interpolation between manual picks to trace each layer along  
267 large amplitude reflections every  $\sim 500 - 700 \text{ m}$  along the traverse. When a layer appears to bifurcate due to  
268 changes in snow accumulation, we continue to trace the layer based on the trajectory of surrounding IRHs.  
269 Each horizon is traced throughout the traverse, except in areas where the attenuated signal makes it too  
270 difficult to interpret (Figure 3). We trace layers for each spur starting at the depth of each layer at the  
271 corresponding firn core location. Layers below the depth of some firn cores are traced from nearby cores that  
272 are deeper or have lower accumulation rates.

273

274 We trace layers between cores using a connect-the-dots approach using the depth-age scale at each firn core.  
275 After tracing layers from one firn core to the next, we check that layers intersect the core location at the  
276 proper depth for the age of our traced IRH. Note that the depths of several layers at Cores 2 – 16 are located  
277 below the bottom depth of those cores. Since these layers are isochronous, they are used to calculate  
278 accumulation rates over appropriate time epochs by using dates obtained from intersections with other cores  
279 (see Figure 3).

280

## 281 **2.6. Accumulation rate calculations and uncertainty**

282 Finally, we calculate snow accumulation rates using the firn core depth-age scales, measured and interpolated  
283 depth-density profiles (Figure 4), and traced IRHs (Figure 2). We calculate the water equivalent accumulation

284 rate  $\dot{b}$  (m w.e. a<sup>-1</sup>) between adjacent IRHs from the depth  $z$  (m) and age  $t$  (year) of each layer, the average  
285 density  $\rho$  (kg m<sup>-3</sup>) between layers, and the density of water  $\rho_w$  (1000 kg m<sup>-3</sup>):

$$286 \quad \dot{b} = \frac{1}{t_2 - t_1} \int_{z_1}^{z_2} \frac{\rho(z)}{\rho_w} dz \quad (3).$$

287  
288 We correct for layer thinning using a Nye (1963) model. The thinning factor has an average value of 0.9993  
289  $\pm$  0.0003 and is multiplied by the accumulation rate for each radar trace. For each radar trace, the thinning  
290 factor,  $\lambda(z)$ , is calculated from the average accumulation rate  $\dot{b}$  (m w.e. a<sup>-1</sup>) of each epoch, average age of the  
291 epoch  $a$  (year), and water equivalent thickness of the GrIS  $H$  (m), from Morlighem et al. (2014):

$$292 \quad \lambda(z) = e^{-\frac{\dot{b}}{H}a} \quad (4).$$

293  
294 Accumulation uncertainty can arise from independent errors in tracing IRHs, errors from incorrectly dating  
295 firn cores, and/or errors in the densities used for converting from separation distance to water equivalent  
296 accumulation rates. To reduce tracing errors, we retraced each IRH along the two main traverse paths four  
297 times apiece. Close inspection of the IRHs reveals that the peaks defining IRHs are within  $\pm$  2 radar samples  
298 (within at most  $\pm$ 0.12 m), and incorrectly jumping to the next IRH would result in an error of at most  $\pm$  10  
299 samples (within  $\pm$ 0.55 m). We chose an epoch between IRHs of 5.0 years from the firn core chemistry depth-  
300 age scales, which corresponds to a maximum tracing error of  $\sim$  $\pm$ 0.11 m a<sup>-1</sup> for each epoch, or a maximum  
301 error of  $\pm$ 0.061 m w.e a<sup>-1</sup> given an average firn density of 0.55 g cm<sup>3</sup> across this dataset.

302  
303 We perform a leave-one-out cross validation to calculate accumulation errors at locations where we do not  
304 have firn core density profiles. Here we choose one of the sixteen firn cores, in addition to the Raven/Dye-2  
305 and Summit cores, to omit from our density interpolation (Figure 4), so that we interpolate density profiles  
306 between adjacent firn cores and a Herron-Langway profile at the missing core location. We find maximum  
307 single-epoch errors of 0.079 m w.e. a<sup>-1</sup> and maximum RMS (1971 – 2016) errors of 0.046 m w.e. a<sup>-1</sup> (Table  
308 1) at the location of missing cores. These differences are approximately twice as large at Cores 1 – 6 than  
309 Cores 7 – 16 due to larger differences between measured and interpolated density profiles, likely a result of  
310 meltwater percolation and ice lenses (Graeter et al., 2018).

311  
312 Similarly, we perform a leave-one-out validation by omitting a firn core density profile location entirely and  
313 interpolating density profiles over a larger distance (e.g. between Core 1 and Core 3). In this case we find  
314 maximum single-epoch errors of 0.057 m w.e. a<sup>-1</sup> and maximum RMS (1971 – 2016) errors of 0.033 m w.e.  
315 a<sup>-1</sup>. Throughout this study, we use our measured density profiles to calculate accumulation rates at core  
316 locations, rather than rely on Herron-Langway density models that would result in larger uncertainties.

317

318

319 We conservatively take our accumulation error from missing density measurements to be 0.079 m w.e. a<sup>-1</sup>.

320 This error highlights the importance of our firn core spacing between 40 – 100 km along the traverse and

321 confirms that the accuracy of future remotely sensed radar accumulation (e.g. IceBridge snow and

322 accumulation radars) estimates depend on precise field-based *in situ* density profiles for accurate

323 accumulation history in the percolation zone. Overly et al. (2016) calculated accumulation rates in the dry

324 snow zone using Herron-Langway profiles within 3.5% of accumulation rates calculated using neutron-probe

325 density profiles. However, here we show that *in situ* measurements, or accurate meltwater percolation

326 modeling (Meyer and Hewitt, 2017), are required to correctly calculate SMB in the percolation zone.

327

328 **Table 1. Difference between accumulation rates at each GreenTrACS core site calculated using Herron-Langway profiles and firn core**  
329 **density information.**

Core	RMS average difference (m w.e. a <sup>-1</sup> )	Max epoch difference (m w.e. a <sup>-1</sup> )	Max Epoch difference (% of acc.)
1	0.046	0.079	20.1
2	0.025	0.061	16.2
3	0.037	0.074	19.9
4	0.028	0.045	10.7
5	0.026	0.054	11.5
6	0.038	0.052	10.0
7	0.015	0.026	5.4
8	0.026	0.045	10.3
9	0.030	0.049	10.9
10	0.019	0.039	8.5
11	0.023	0.035	5.0
12	0.018	0.027	8.2
13	0.025	0.031	10.7
14	0.019	0.027	8.2
15	0.010	0.016	5.3
16	0.014	0.025	8.2

330

331 We assume uncertainty in dating the firn cores from annual variations in chemistry to be ±0.5 years (Buchardt

332 et al., 2012). At the lowest accumulation rate locations, the smallest distance between layers is 0.15 m w.e.

333 over an epoch of 4.91 years. This gives an uncertainty in accumulation rates due to dating of at most ~±0.03

334 m w.e. a<sup>-1</sup>. The error associated with measuring *in situ* firn density has been estimated to be 1.4% (Karlöf et

335 al., 2005). However, following Hawley et al. (2014) and Lewis et al. (2017), we conservatively assume that

336 our measurements have a density measurement error of up to twice this large, corresponding to a maximum  
337 accumulation error of  $\pm 0.014$  m w.e.  $a^{-1}$ .

338

339 We calculate the total uncertainty from formal error propagation (following Bevington and Robinson, 1992)  
340 from the average accumulation rate  $\dot{b} = 0.385$  m w.e.  $a^{-1}$ , average thickness between IRHs  $\Delta h = 3.56$  m,  
341 uncertainty in tracing  $\delta h$ , average firm density  $\rho = 0.550$  g  $cm^3$ , uncertainty in density measurements  $\delta\rho$ ,  
342 average time period between IRHs  $\Delta t$ , and uncertainty in core dating  $\delta t$ . We find the total accumulation rate  
343 uncertainty for each epoch to be  $0.071$  m w.e.  $a^{-1}$  from equation 5.

$$344 \sigma_{epoch} = \sqrt{\dot{b}^2 \left( \left( \frac{\delta h}{\Delta h} \right)^2 + \left( \frac{\delta t}{\Delta t} \right)^2 + \left( \frac{\delta \rho}{\rho} \right)^2 \right)} \quad (5)$$

345

346 Due to the random and non-systematic nature of these errors, we can assume that they are unlikely to  
347 contribute to a regional or temporal accumulation rate bias. To calculate uncertainty for accumulation rates  
348 averaged over multiple epochs ( $\sigma_{n-epochs}$ ) we divide our uncertainty  $\sigma_{epoch}$  by the square root of the number  
349 of traced layers ( $n$ ) at that location.

$$350 \sigma_{n-epochs} = \frac{\sigma_{epoch}}{\sqrt{n}} \quad (6).$$

351

## 352 **2.7. Model comparison**

353 We compare our GreenTrACS accumulation results with annual outputs from Box et al. (2013; hereafter  
354 “Box13”; 1840 – 1999), the Fifth Generation Mesoscale Model (Polar MM5; 1958 – 2008; Burgess et al.,  
355 2010), MAR (1948 – 2015; Fettweis et al., 2016), and the Regional Atmospheric Climate Model (RACMO2;  
356 1958 – 2015; Noël et al., 2018) over common time periods. Grid cell sizes for these model outputs are 5 km,  
357 3 km, 5 km, and 1 km, respectively. For each radar trace we calculate statistically significant differences (at  
358  $\alpha = 0.05$ ) using a two sample t-test with the GreenTrACS accumulation records for each epoch and RCM  
359 accumulation rates for each common year. Additionally, we compare our GreenTrACS accumulation rates  
360 with an accumulation map kriged from 295 firm cores and 20 coastal weather stations (Bales et al., 2009;  
361 hereafter “Bales09”). We perform the same two sample t-test with the reported Bales09 uncertainty of  $0.092$   
362 m w.e.  $a^{-1}$  (Bales et al., 2009).

363

## 364 **2.8. Accumulation trends**

365 To investigate recent changes in GrIS accumulation rates, we calculate trends in accumulation rates across  
366 our GPR and GreenTrACS firm core dataset. We fit a linear model to the accumulation rate time series for

367 each radar trace and analyze the trend for both slope and statistical significance. Likewise, we calculate trends  
368 and their statistical significance for total precipitation (snowfall + rainfall) for MAR and RACMO2 grid cells  
369 from 1996 through the end of both models' temporal coverage. We can compare these results with our  
370 accumulation trends since precipitation and accumulation rates are nearly identical above the equilibrium  
371 line altitude, due to zero runoff and negligible sublimation within the percolation zone.

## 372 **2.9. Storm track changes**

373 To investigate the potential role of changing storm tracks in precipitation changes over the Western GrIS, we  
374 utilize the updated Serreze (2009) storm track database. This database contains six-hour interval positions of  
375 extratropical cyclone storm centers on a  $2.5^\circ$  grid. These centers are defined when a gridpoint sea level  
376 pressure is surrounded by gridpoints at least 2 mb higher than the central point (Serreze, 2009). We calculate  
377 the total number of days in which a storm center is located within our region of interest for each season. To  
378 determine statistical significance, we run a two sample t-test on the number of storms in our region of interest  
379 between 1958 – 1996 compared with 1996 – 2016.

## 380 **3. Results and discussion**

### 381 **3.1. Firn core and GPR accumulation records**

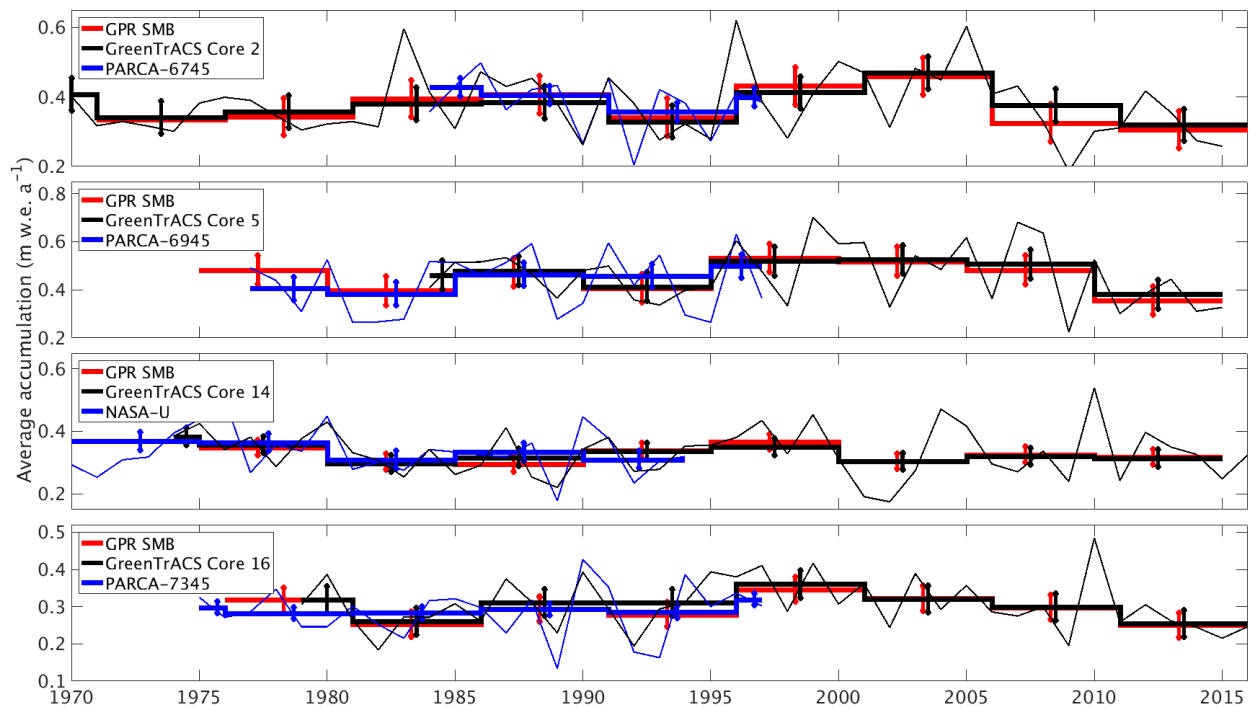
382 Figure 1 displays the mean accumulation rates at each location along the traverse route, with higher  
383 accumulation rates along the main traverse and lower accumulation rates at higher elevations of the ice sheet  
384 interior, broadly consistent with previously published accumulation rate compilations (e.g. Bales et al., 2009)  
385 and RCM output (Box et al., 2013; Burgess et al., 2010; Fettweis et al., 2016; Noël et al., 2018). We analyze  
386 localized differences between GPR derived accumulation rates and these RCMs in Section 3.3. There is an  
387 especially high accumulation rate zone near Core 11 ( $0.685 \text{ m w.e. a}^{-1}$ ), nearly double the accumulation rate  
388 at Core 10 ( $0.453 \text{ m w.e. a}^{-1}$ ) and Core 12 ( $0.327 \text{ m w.e. a}^{-1}$ ), respectively situated only 43 km northwest and  
389 73 km southwest of Core 11. In the GPR data, the number of traceable IRHs is highest towards the interior  
390 of the ice sheet and lowest in warmer areas towards the coast and in the south, where refrozen percolated  
391 melt water from enhanced surface melt attenuates the radar signal and reduces the number of observable  
392 IRHs (Brown et al., 2011; Figure 3).

### 393 **3.2. Validation with past measurements**

394 We validate our accumulation record with published core records from the PARCA campaign and  
395 accumulation data from the NASA IceBridge program. The locations of GreenTrACS Core sites 2, 5, 9, 10,  
396 11, 14, 15, and 16 were chosen to reoccupy PARCA core locations 6745, 6945, 7147, 7247, 7249, NASA-



397 U, 7347, and 7345, respectively. These GreenTrACS cores overlap with the accumulation history of each  
 398 PARCA core and extend the record from 1997/1998 to 2016/2017. Annual and epoch-averaged accumulation  
 399 rates derived from GreenTrACS firm cores are within uncertainty ranges of those determined from  
 400 corresponding PARCA cores during the period of overlap. Averaging accumulation rates over five year  
 401 epochs reduces noise in year-to-year accumulation variability. Figure 5 compares the accumulation records  
 402 from PARCA sites 6745, 6945, 7345, and NASA-U to their corresponding GreenTrACS cores,  
 403 demonstrating that each pair of cores has similar long-term mean accumulation rates and nearly identical  
 404 decadal variability. Thus, we have confidence in firm core derived accumulation rates that are used in  
 405 subsequent GPR calculations of accumulation rates throughout the GreenTrACS traverse.  
 406



407  
 408 **Figure 5. Accumulation rates from GPR and collected firm cores (this study) compared with cores from the PARCA Campaign. Thin**  
 409 **lines represent annual PARCA (blue) and GreenTrACS (black) firm core accumulation rates, while thick lines are 5-year averages over**  
 410 **corresponding GPR epochs. Error bars represent one standard deviation over each epoch. GPR and PARCA accumulation rate averages**  
 411 **and decadal trends are statistically indistinguishable.**

412  
 413 Average (1966 – 2016) GPR accumulation rates are statistically indistinguishable with average (1962 – 2014)  
 414 IceBridge Accumulation Radar measurements analyzed by Lewis et al. (2017), with an RMS difference of  
 415  $0.039 \pm 0.033$  m w.e. a<sup>-1</sup> ( $6.0 \pm 9.6\%$ ) along a total of 562.5 km of overlap (Figure 6). The disagreement is  
 416 largest at lower elevations, where Herron-Langway profiles used in Lewis et al. (2017) differ the most from  
 417 GreenTrACS firm core density profiles in the upper 30 m of firm, demonstrating the importance of field  
 418 observations for calibration and validation. The close agreement at higher elevations is illustrated in Figure

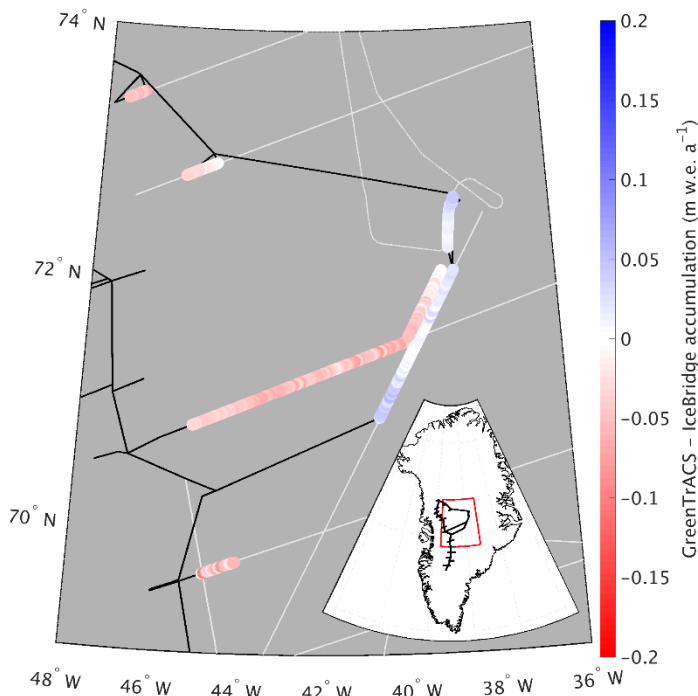
419 7a, where our GreenTrACS accumulation measurements are statistically indistinguishable from the IceBridge  
420 radar-derived accumulation rates (Lewis et al., 2017) along the 285 km A – A’ transect on Figure 1. Notice  
421 that the uncertainty in GreenTrACS accumulation rates progressively decreases higher in the percolation  
422 zone and into the dry snow zone (towards the right in Figure 7) along this transect as density becomes less  
423 heterogeneous from fewer melt layers (Graeter et al., 2018) and IRHs become easier to trace.

424

425 Similarly, our 2011-2016 accumulation rates are statistically indistinguishable from average 2009 – 2012  
426 IceBridge snow radar measurements analyzed by Koenig et al. (2016), with an RMS difference of  $0.049 \pm$   
427  $0.096$  m w.e.  $a^{-1}$  ( $14.0 \pm 27.7\%$ ) along a total of 69.7 km of overlap (not shown). Koenig et al. (2016) use a  
428 different radar system on an airborne platform and are able to calculate annual accumulation rates at  
429 elevations below 2000 m a.s.l., however the GreenTrACS accumulation record covers a longer temporal  
430 duration than the data from that study.

431

432



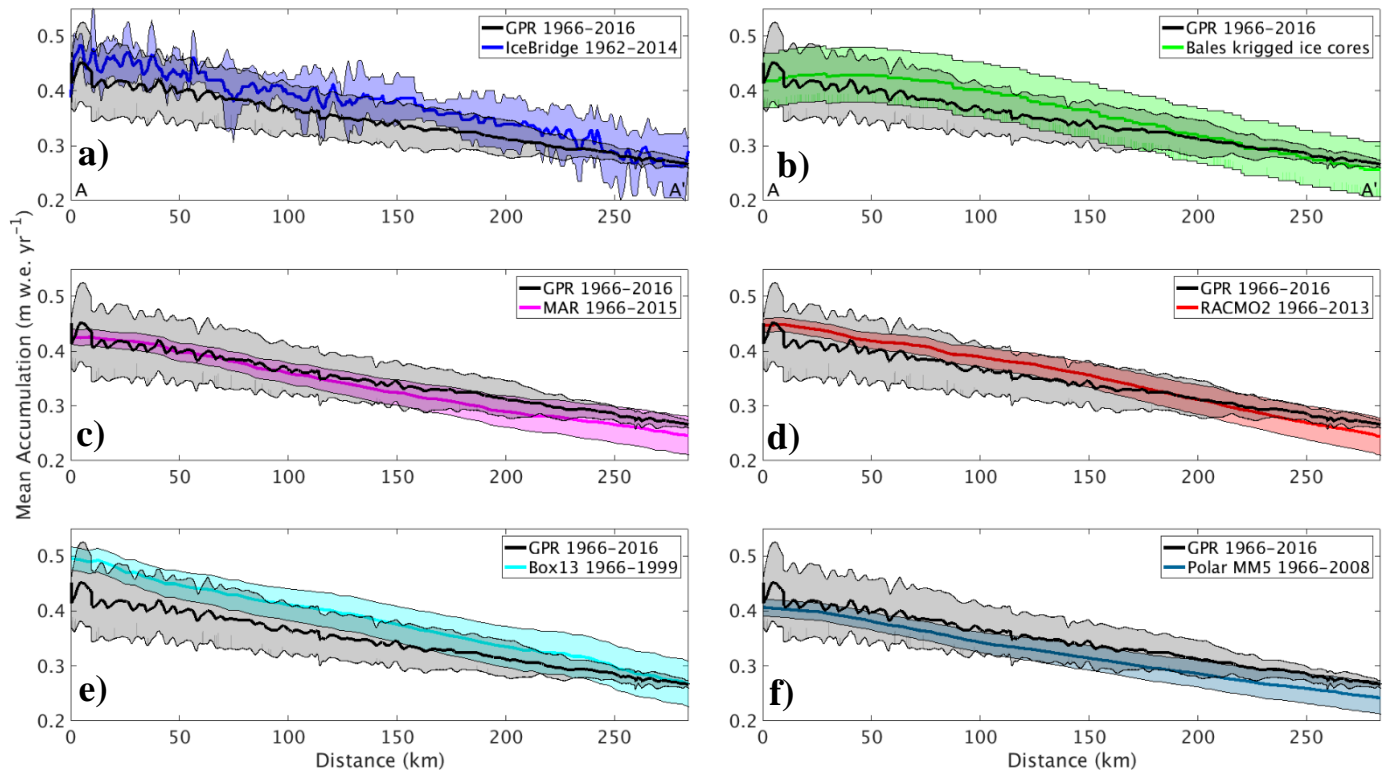
433

434 **Figure 6. Difference between averaged (1966 – 2016) GreenTrACS accumulation and average (1962 – 2014) IceBridge Accumulation**  
435 **Radar rates from Lewis et al. (2017) across all 562.5 km of overlap. Spatially overlapping section of 2016 and 2017 traverses displayed**  
436 **as adjacent tracks. Also showing extent of GreenTrACS traverse (black) and IceBridge accumulation radar (grey). Inset shows map**  
437 **location with respect to GreenTrACS traverse (black).**

438

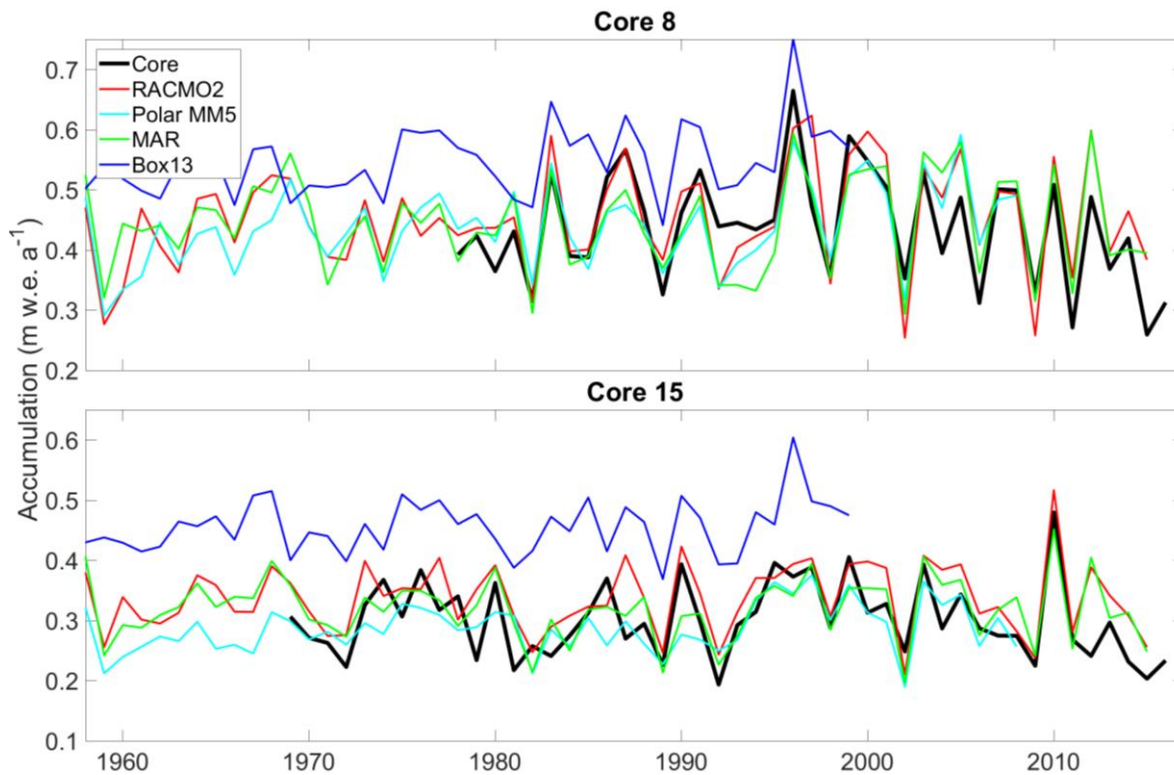
439 **3.3. Comparison to modelled accumulation**

440 We assess differences between RCM accumulation output and GreenTrACS accumulation records at each  
 441 firm core site, two of which are shown in Figure 8. In general, year-to-year correlations between GreenTrACS  
 442 firm core accumulation records and RCM output for the corresponding grid cell are strong, positive, and  
 443 statistically significant (Table 2). On average, GreenTrACS firm cores' correlation coefficient with MAR  
 444 output is 0.718, with PolarMM5 is 0.701, with Box13 is 0.607, and with RACMO2 is 0.763. Every correlation  
 445 is statistically significant at  $p < 0.05$  except for Cores 7 and 11 with Box13. We do not report a correlation  
 446 coefficient for Core 11 and Box13 because they only share two common years. Temporal correlation  
 447 coefficients remain high even at locations with large magnitude differences between RCM output and firm  
 448 core accumulation rates. For example, the Box13 model overestimates accumulation rates at Core 15 by  $0.15$   
 449  $\pm 0.05$  m w.e.  $a^{-1}$ , on average, but the model output has a correlation coefficient of 0.48 with Core 15 (Table  
 450 2) and matches years of high accumulation rates (e.g. 1987, 1990, and 1996) and low accumulation rates (e.g.  
 451 1981, 1989, 1992).



452  
 453 **Figure 7. Average GreenTrACS GPR accumulation rates (black) compared with a) IceBridge accumulation radar, b) Bales09 krigged**  
 454 **ice core map, c) MAR, d) RACMO2, e) Box13, and f) Polar MM5. GPR measurements are statistically indistinguishable from each of**  
 455 **the other measurements along this 285 km transect in the dry snow zone (A – A' on Figure 1).**

456



457

458 **Figure 8.** Accumulation record at GreenTrACS Core 8 and Core 15 (black) compared with RCM output from RACMO2 (red), Polar  
 459 MM5 (cyan), MAR (green), and Box13 (blue). We find statistically significant Pearson correlation coefficients between GreenTrACS  
 460 and RCM accumulation rates for these cores (see Table 2).

461

462 **Table 2.** Pearson correlation coefficients between accumulation rate time series from firn cores and co-located RCM output over their  
 463 common time period<sup>#</sup>.

	Available data period	MAR	PolarMM5	Box13	RACMO2
Core1	1966 – 2016	<b>0.70</b>	<b>0.66</b>	<b>0.56</b>	<b>0.73</b>
Core2	1969 – 2016	<b>0.75</b>	<b>0.77</b>	<b>0.62</b>	<b>0.79</b>
Core3	1971 – 2016	<b>0.72</b>	<b>0.69</b>	<b>0.63</b>	<b>0.74</b>
Core4	1977 – 2016	<b>0.79</b>	<b>0.74</b>	<b>0.72</b>	<b>0.72</b>
Core5	1984 – 2016	<b>0.81</b>	<b>0.80</b>	<b>0.60</b>	<b>0.79</b>
Core6	1985 – 2016	<b>0.76</b>	<b>0.76</b>	<b>0.65</b>	<b>0.83</b>
Core7	1993 – 2016	<b>0.81</b>	<b>0.82</b>	0.61	<b>0.73</b>
Core8	1978 – 2017	<b>0.78</b>	<b>0.77</b>	<b>0.69</b>	<b>0.81</b>
Core9	1984 – 2017	<b>0.68</b>	<b>0.75</b>	<b>0.74</b>	<b>0.79</b>
Core10	1984 – 2017	<b>0.88</b>	<b>0.80</b>	<b>0.80</b>	<b>0.80</b>
Core11	1997 – 2017	<b>0.75</b>	<b>0.59</b>	N/A	<b>0.75</b>
Core12	1962 – 2017	<b>0.6</b>	<b>0.54</b>	<b>0.53</b>	<b>0.64</b>
Core13	1955 – 2017	<b>0.51</b>	<b>0.62</b>	<b>0.37</b>	<b>0.76</b>
Core14	1974 – 2017	<b>0.70</b>	<b>0.62</b>	<b>0.46</b>	<b>0.74</b>
Core15	1969 – 2017	<b>0.68</b>	<b>0.63</b>	<b>0.48</b>	<b>0.75</b>
Core16	1979 – 2017	<b>0.79</b>	<b>0.77</b>	<b>0.66</b>	<b>0.88</b>

464 <sup>#</sup>Statistically significant correlations ( $p < 0.05$ ) are bold

465

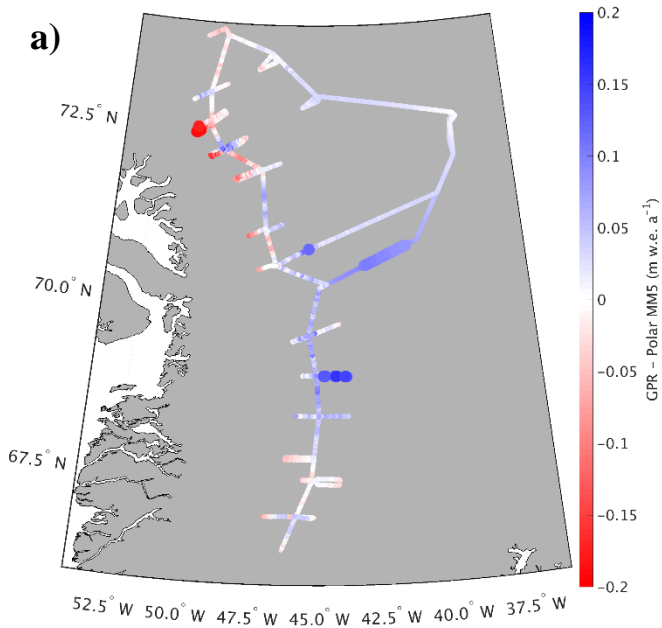
466 We also assess spatial differences between GreenTrACS accumulation rates and mean RCM accumulation  
 467 rates averaged over several decades (Table 2). Figure 9 shows that differences between GreenTrACS

468 accumulation rates and RCM output increase in magnitude, become more spatially heterogeneous, and vary  
469 by model at lower elevations of the ice sheet where topographic variations are larger and surface melt  
470 increases. Averaged over all 4436 km of the traverse, the RMS difference ( $\pm 1\sigma$ ) between each model and  
471 GreenTrACS accumulation rates over corresponding data periods (Table 2) is  $0.068 \pm 0.065$  (MAR),  $0.056$   
472  $\pm 0.055$  (RACMO2),  $0.082 \pm 0.070$  (Box13),  $0.048 \pm 0.045$  (Polar MM5), and  $0.048 \pm 0.045$  m w.e.  $a^{-1}$   
473 (Bales09). We find that RCM differences from GreenTrACS accumulation rates are small in the dry snow  
474 zone (Figure 9). For example, Figure 7 shows that average GreenTrACS accumulation measurements from  
475 1966 – 2016 along the A – A' transect in Figure 1 are statistically indistinguishable from those derived from  
476 the Bales09 krigged ice core map (Figure 7b), MAR (1966 – 2015; Figure 7c), RACMO2 (1966 – 2013;  
477 Figure 7d), Box13 (1966 – 1999; Figure 7e), and Polar MM5 (1966 – 2008; Figure 7f).

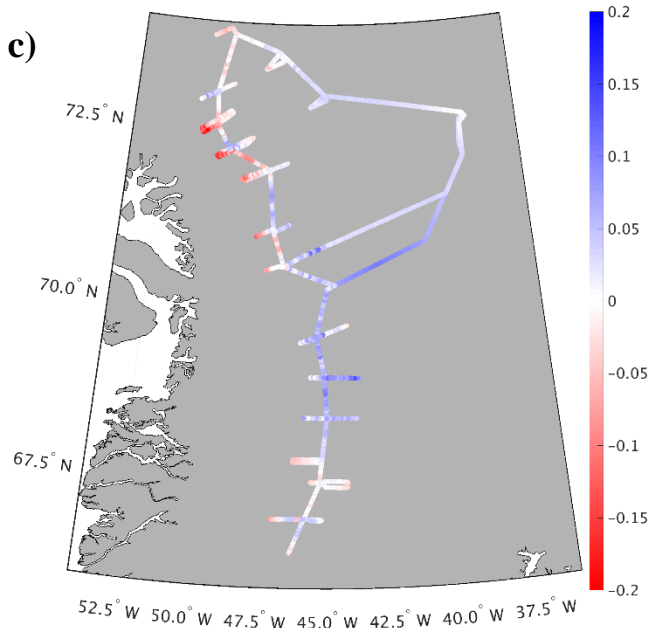
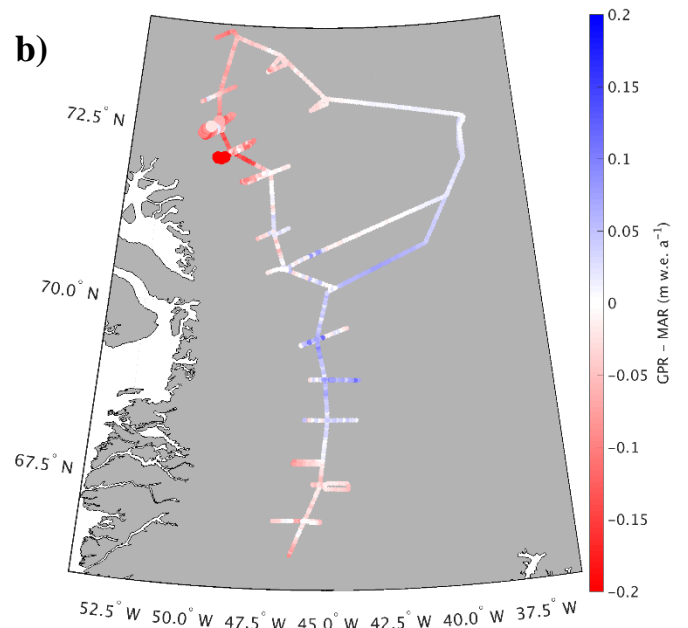
478  
479 However, the high spatial resolution of our dataset shows significant accumulation variability not captured  
480 in model output (Figure 9). For example, Polar MM5 and MAR both underestimate accumulation rates  
481 between Core 4 and Summit, while overestimating accumulation rates to the west of Cores 10 – 12. Likewise,  
482 RACMO2 overestimates accumulation rates between Raven/Dye-2 and Core 5 by 0.03 to 0.08 m w.e.  $a^{-1}$  and  
483 shows statistically significant differences east of Cores 11 and 12. Bales09 accurately calculates  
484 accumulation rates along most of the 2016 traverse, but overestimates accumulation rates west of Cores 11  
485 and 12 by  $0.135 \pm 0.041$  m w.e.  $a^{-1}$ . Finally, Box13 overestimates accumulation rates along many of the  
486 western spurs and has statistically significant overestimations of 0.1 to 0.4 m w.e.  $a^{-1}$  between Cores 10 and  
487 16. Box13 overestimates 67.8% of the data in the Core 10 – 16 region by at least 0.1 m w.e.  $a^{-1}$ , and 6.6% of  
488 that data by at least 0.2 m w.e.  $a^{-1}$ .

489  
490 Our study is almost entirely contained within drainage basin E from Vernon et al. (2013), who note that basin  
491 E is the only major Greenland drainage basin with no statistically significant differences in SMB between  
492 the four RCMs. However, differences of 0.1 to 0.4 m w.e.  $a^{-1}$  exist when we look at a local (sub-drainage-  
493 basin) scale for each model. All four of the RCMs overestimate accumulation rates along the western spur of  
494 Core 11 and they all underestimate accumulation rates along the eastern spur of Core 5 (Figure 9).

495

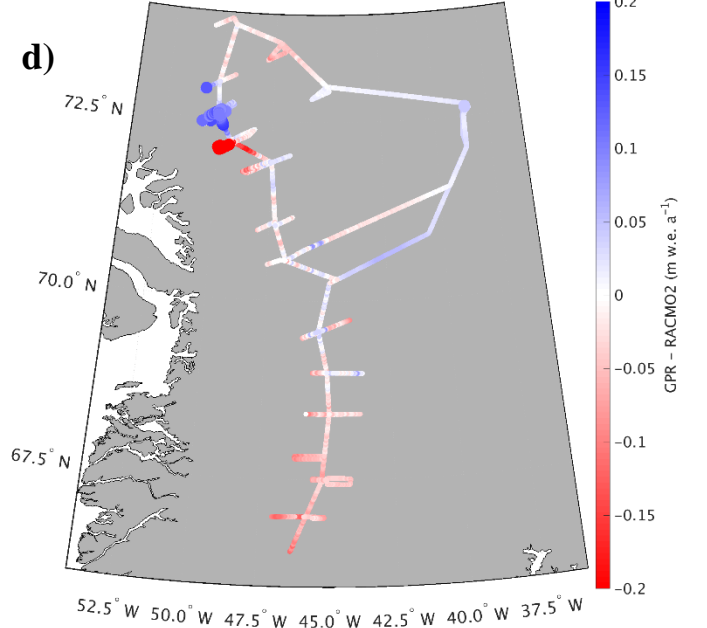


496

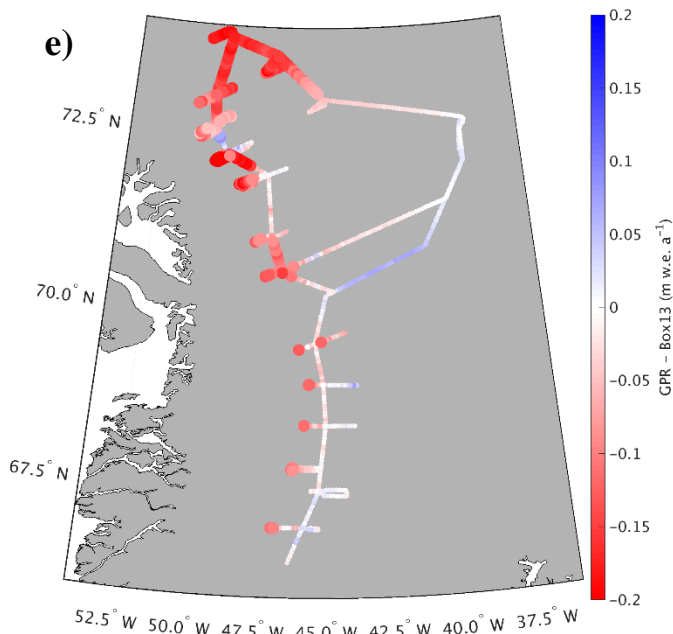


497

498







499 **Figure 9. Differences between GreenTrACS accumulation rates and a) Polar MM5, b) MAR, c) Bales09, d) RACMO2, and e) Box13**  
 500 **accumulation rates averaged over the corresponding time periods. Large dots show statistically significant differences from**  
 502 **GreenTrACS accumulation rates.**

503  
 504 In summary, the RCMs do an excellent job of calculating accumulation rates averaged over this drainage  
 505 basin, with RMS values between 0.048 and 0.082 m w.e. a<sup>-1</sup>, but there are larger differences of 0.1 to 0.4 m  
 506 w.e. a<sup>-1</sup> between model and GPR accumulation rates on local scales. Differences between GreenTrACS and  
 507 RCM accumulation rates are largest in areas concurrent with the fewest, shortest, and/or most outdated *in*  
 508 *situ* measurements. For example, the GPR vs. model differences near Cores 11, 12, and 13 are relatively large  
 509 for all RCMs, despite Core 11 being co-located with PARCA 7249. However, the PARCA cores were  
 510 collected over 20 years ago, and Core 11 only spanned 7 years because of the high accumulation rate at that  
 511 site. This highlights the importance of collecting updated field-based measurements to calibrate remotely  
 512 sensed data and RCM output.

### 514 3.4. Accumulation temporal trends

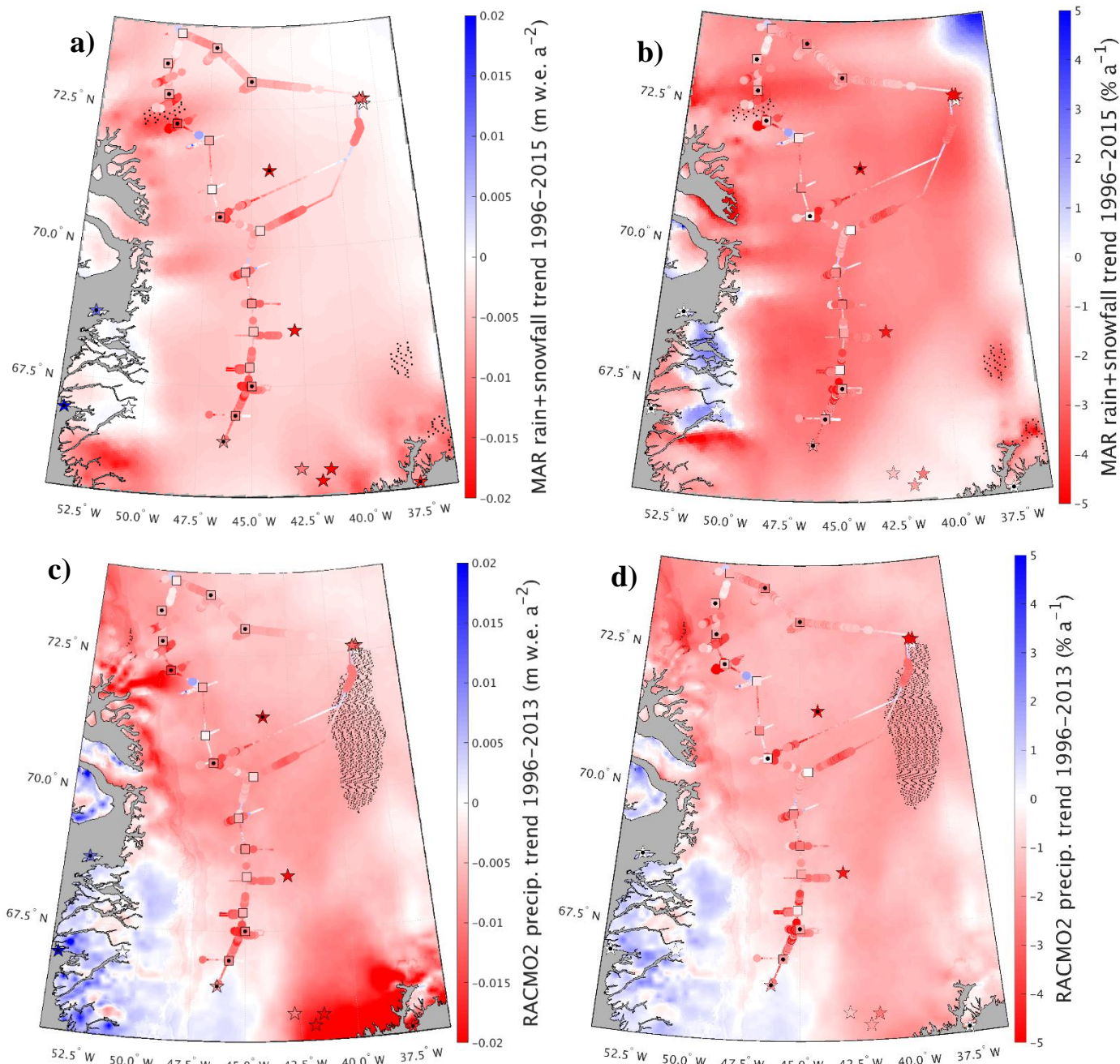
515 In most locations, there are no statistically significant trends in the GreenTrACS accumulation record from  
 516 1966 through the mid-1990s. However, a changepoint analysis (Lavielle, 2005) reveals that accumulation  
 517 rates in the Western GrIS percolation zone changed significantly after the 1995 – 1996 accumulation year.  
 518 Since 1996, our record indicates a statistically significant average accumulation rate decrease of  $0.009 \pm$   
 519  $0.005$  m w.e. a<sup>-2</sup>, or  $2.4 \pm 1.5$  % a<sup>-1</sup>, from 1996 to 2017. Although we observe fewer statistically significant  
 520 accumulation trends when we expand this analysis to include the entire temporal duration for each firn core,  
 521 the sign of the trend at each core site does not change.

522

523 In Figure 10, we compare the negative accumulation trend in the GreenTrACS record (1996 – 2016) to best-  
524 fit linear trends in total precipitation (rain + snowfall) across the ice sheet in MAR and RACMO2 simulations  
525 over the 1996 – 2015 and 1996 – 2013 periods, respectively. Also shown in Figure 10 are 1996 – 2016  
526 accumulation trends for all 16 GreenTrACS firn cores (squares), accumulation trends from ACT10A (1996  
527 – 2010), ACT10B (1996 – 2010), ACT10C (1996 – 2010), D4 (1991 – 2002), D5 (1991 – 2002), Katie (1991  
528 – 2002), Sandy (1991 – 2002), and Summit 2010 (1991 – 2010) ice/firn cores (stars on ice sheet), and  
529 precipitation trends from coastal weather stations (Mernild et al., 2014; stars on coast). Statistically  
530 significant trends ( $p < 0.05$ ) in core data are indicated by black dots, while statistically significant trends in  
531 the MAR and RACMO2 output are stippled in black.

532

533 We find strong agreement between the accumulation rate decrease in the GreenTrACS record and widespread  
534 precipitation decreases in the RCMs over the study area (Figure 10). On average, the RCMs have a more  
535 negative precipitation trend than the GreenTrACS record by  $0.003 \pm 0.005$  m w.e.  $a^{-2}$  ( $0.3 \pm 0.77\%$ ) for MAR  
536 and  $0.002 \pm 0.005$  m w.e.  $a^{-2}$  ( $0.45 \pm 1.22\%$ ) for RACMO2. Vernon et al. (2013) show a melt-driven decrease  
537 in SMB across this drainage basin of 31.1% (ECMWFd), 61.6% (RACMO2), 76.5% (MAR), and 33.5%  
538 (Polar MM5) for the 1996 – 2008 period. The negative precipitation trends of  $2.4 \pm 1.5$  %  $a^{-1}$  (Figure 10d)  
539 indicate a total of 2539.4 fewer Gt of precipitation and a total of 5159.1 additional Gt of melt (not shown)  
540 over 1996 – 2013 across the GrIS. Thus, our analysis suggests that a significant decline in snow accumulation  
541 rates contributes to declining SMB throughout the Western GrIS over recent decades, in addition to  
542 increasing surface melt from rising temperatures (van den Broeke et al., 2009, 2016).



543

544

545 **Figure 10.** Best fit linear trends for each grid cell showing magnitude (left) and percent (right) changes in total precipitation for a) and  
 546 b) MAR (1996 – 2015) and c) and d) RACMO2 (1996 – 2013). Statistically significant RCM grid cell trends are stippled black. Also  
 547 shown are accumulation trends for GreenTrACS firn cores (squares), ACT10A, ACT10B, ACT10C, D4, D5, Katie, Sandy, Summit 2010,  
 548 and Raven/Dye-2 cores (stars on ice sheet) and precipitation trends from Mernild et al (2014; stars on coast) with statistically significant  
 549 trends indicated by black dots.

550

551 **3.5. Effects of melt on accumulation trends**

552 Increased melt throughout the 1996 – 2016 period is a confounding variable when analyzing trends in  
 553 accumulation rates. With increased melt over the past several decades in this region, meltwater percolates  
 554 down through several years of firn (Benson, 1962; Graeter et al., 2018; Harper et al., 2012; Wong et al.,

2013). This movement of mass into lower years can artificially increase the mass balance at depth and lower the mass balance during the most recent years, which have not experienced as much meltwater percolation from more recent annual layers. Therefore, it is necessary to evaluate the degree to which the recent accumulation rate decrease in the GreenTrACS record is biased by the recent increase in surface melt and percolation.

On average, we find larger negative accumulation trends ( $-7 \times 10^{-3}$  to  $-10 \times 10^{-3}$  m w.e.  $a^{-2}$ ) at the lower latitude cores that experience more melt, supporting the hypothesis that meltwater percolation and refreezing are enhancing the negative accumulation trend. However, several other lines of evidence support a negative accumulation trend in the study area since 1996. First, we find statistically significant negative accumulation trends at Cores 10, 11, 12, 13, 15, and 16, each of which experience  $<1.6$  cm  $a^{-1}$  of meltwater percolation on average. Additionally, we have confidence that GreenTrACS accumulation trends reported here are not artifacts of meltwater percolation because both MAR and RACMO2 have similar trends in precipitation (Figure 10). Finally, we evaluate the maximum effect meltwater percolation could have on GreenTrACS accumulation trends over 1996 – 2016. The largest measured melt layer from our sixteen ice cores occurred during 2003 – 2004 in Core 1 and contains 0.364 m of ice, equivalent to 0.333 m w.e. (Graeter et al., 2018). We add this percolation to nine years' of accumulation rates using a sine wave (percolation magnitude 0, 0.5, 1, 0.5, 0, -0.5, -1, -0.5, 0), square wave (0, 0, 0, 1, 1, 1, 0, 0, 0), and triangle wave (0, 0.25, 0.5, 0.75, 1, 0.75, 0.5, 0.25, 0) weighted kernel, before re-computing hypothetical accumulation trends over the same time period with additional meltwater percolation. Regardless of the wave-type choice, re-calculated trends remain within a factor of two of the original SMB trends and do not change sign with additional percolation.

### 3.6. Atmospheric circulation drivers of the recent accumulation decline

Our analysis indicates that snow accumulation rates have been declining in Western Greenland since 1996, despite significant warming and resulting increases in saturation vapor pressure from the Clausius-Clapeyron relationship. Instead, precipitation decreases over Western Greenland likely result from changes in atmospheric and/or oceanic circulation. Mernild et al. (2014) and Auger et al. (2017) found that the positive phase of the Atlantic Multidecadal Oscillation (AMO) is associated with a precipitation increase over interior and Southwestern Greenland based on ice core records and the Japanese Meteorological Agency 55 Year Reanalysis (JRA-55; Kobayashi et al., 2015), respectively. In direct contrast with these findings, the decline in Western Greenland accumulation rates documented in the GreenTrACS record began in the mid-1990s, contemporaneous with a switch to the AMO positive phase.

588 We hypothesize that the differences between our results and those of Auger et al. (2017) and Mernild et al.  
589 (2014) stem from different causes. Auger et al. (2017) validated the reanalysis data by demonstrating that  
590 JRA-55 precipitation at Nuuk, Greenland is significantly correlated with Nuuk station data from 1958 – 2013.  
591 Furthermore, coastal precipitation in Western Greenland is strongly and significantly ( $p < 0.05$ ) correlated  
592 with precipitation over the interior Western GrIS in the JRA-55 dataset (not shown). However, Mernild et al.  
593 (2014) found that coastal Greenland precipitation is anti-correlated with ice core accumulation records from  
594 the interior GrIS from 1900 to 2000. This suggests that JRA-55 precipitation data, which is not constrained  
595 by ice core accumulation records, should be interpreted with caution over the interior GrIS. Mernild et al.  
596 (2014) concluded that positive AMO conditions favor higher precipitation over the interior GrIS based on  
597 the previous positive AMO phase (1920s to mid-1960s), contrasting with lower accumulation rates during  
598 the negative AMO phases (mid-1960s to mid-1990s and prior to the 1920s). However, Mernild et al. (2014)  
599 state that the ice core composite record in their analysis may be biased from 1995 – 2000, and they do not  
600 analyze precipitation trends after 2000. Thus, the decline in Western GrIS accumulation rates documented in  
601 the GreenTrACS cores during the latest positive AMO phase from 1996 to 2017 was not captured in the  
602 Mernild et al. (2014) analysis. Our results suggest that factors other than the AMO are behind the decline in  
603 Western GrIS accumulation rates since 1996.

604  
605 We find that the decrease in accumulation rates over the Western GrIS is associated with a significant  
606 decrease in the number of storm-days since 1996. The GreenTrACS region experienced an average of  $115.8$   
607  $\pm 15.3$  storm-days per year over 1958 – 1996 and  $96.2 \pm 27.3$  storm-days per year over 1996 – 2016. A two  
608 sample t-test indicates that this 17% decline in storm-days is statistically significant ( $p < 0.001$ ). The largest  
609 decrease in storm-days (25%) over the GreenTrACS region occurred during summer, with  $56.4 \pm 6.1$  storm-  
610 days per summer from 1958 – 1996 and  $42.3 \pm 17.4$  storm-days per summer from 1996 – 2016 ( $p < 0.0001$ ;  
611 Figure 11b). We also find an increase in the number of storm-days in the Northwestern GrIS near Thule (not  
612 shown).

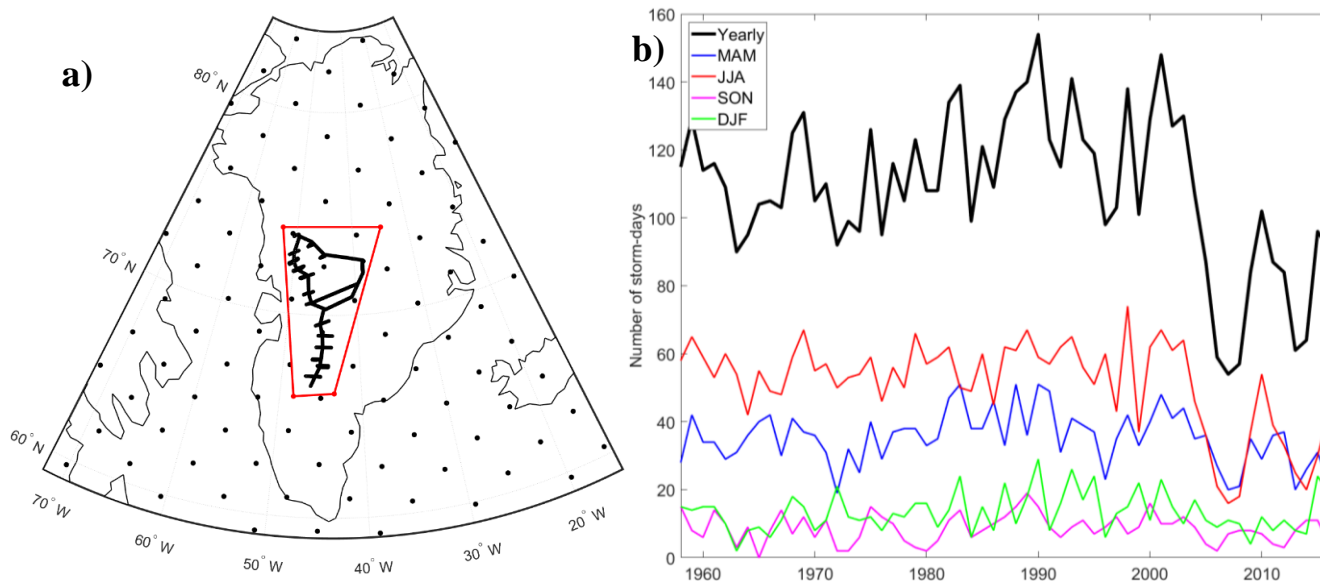
613  
614 The decline in summer storm-days indicates a relationship with well-documented stronger summer blocking  
615 over Greenland over the past two decades (Hanna et al., 2013; McLeod and Mote, 2016), with a positive  
616 Greenland Blocking Index (GBI) during 17 out of 21 summers between 1996 – 2016 (Hanna et al., 2016).  
617 The June – August GBI had a statistically significant positive trend of 1.87 (unitless; normalized to 1951 –  
618 2000) from 1991 – 2015 (Hanna et al., 2016). The summertime 500 mbar geopotential height increased 50 –  
619 70 m over the 1996 – 2016 period compared with the 1979 – 1996 baseline (Figure 11c), indicating stronger  
620 blocking that we suggest likely reduced precipitation over the central GrIS by deflecting storms poleward  
621 from the Greenland interior. This is consistent with an observed  $0.9 \pm 0.3\%$   $a^{-1}$  decrease in JJA cloud cover

622 over Greenland from 1995-2009, with the largest decreases in the GreenTrACS region (Hofer et al., 2017).  
623 Furthermore, we find a strong negative correlation between ERA-Interim 1979 – 2015 June – August (JJA)  
624 GBI and JJA precipitation in both MAR (Figure 11d) and RACMO2 (not shown) across the central and  
625 southern GrIS. These results suggest that the blocking-induced accumulation rate decline observed in the  
626 GreenTrACS region is representative of a broader pattern over the GrIS, with the exception of Northwest  
627 Greenland where poleward blocking has increased storm-days (not shown) and accumulation rates (Figure  
628 11d).

629  
630

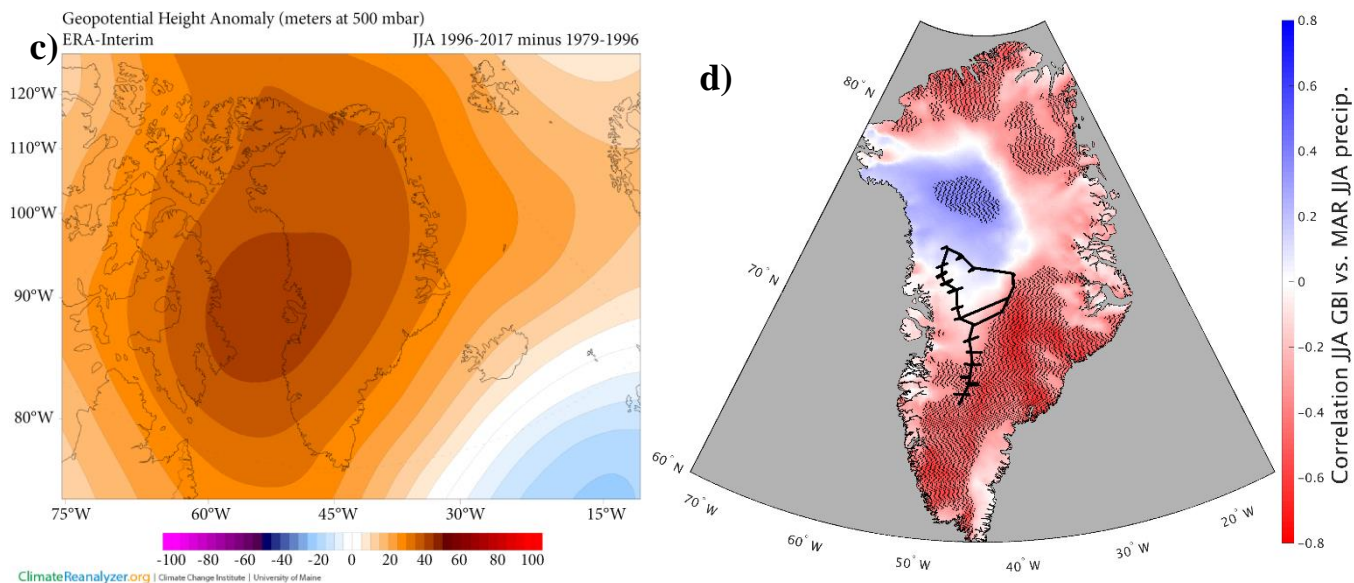
631 The effect of summertime Greenland blocking has previously been discussed primarily in the context of  
632 increasing surface melt (Hanna et al., 2013; Ballinger et al., 2017; Hanna et al., 2018; Hofer et al., 2017),  
633 while the effect of blocking on precipitation has received less attention (Hanna et al., 2013; McLeod and  
634 Mote, 2016). Our results highlight that stronger summer blocking reduces GrIS SMB through both an  
635 increase in surface melting and a decrease in accumulation rates. Stronger summer blocking has been tied to  
636 an observed increase in surface melt since 1996 across the Western GrIS percolation zone (Graeter et al.,  
637 2018), and to the July 2012 melt event, during which 98.6% of the GrIS experienced melt (Nghiem et al.,  
638 2012). We show here with *in situ* data that snow accumulation rates have declined in this same region as  
639 strong blocking has decreased the number of summer storm-days. Presently, none of the GBI outputs from  
640 the Coupled Model Intercomparison Project 5 (CMIP5) suite of global climate models accurately capture the  
641 recent summer GBI increase (Hanna et al., 2018). Improved predictions of summertime Greenland blocking  
642 under future anthropogenic forcing scenarios are therefore critical for accurately predicting Greenland SMB  
643 and its contribution to sea level rise.

644



645





646  
647

648 **Figure 11. a) (Serreze, 2009) gridded storm track dataset showing location of GreenTrACS traverse and inquiry box. b) Total number of storm-days within inquiry box for annual and seasonal periods. Horizontal black lines show a decrease in 1958 – 1996 to 1996 – 2016 average number of storm-days within this region. c) 500 mbar geopotential height change over Greenland showing 1996 – 2016 minus 1979 – 1996 for the summer season. Image obtained using Climate Reanalyzer (<http://cci-reanalyzer.org>), Climate Change Institute, University of Maine, United States. d) Correlation between June – August Greenland Blocking Index and MAR June – August precipitation. Statistically significant RCM grid cell correlations are stippled black. GreenTrACS traverse is shown in black.**

#### 654 4. Conclusions

655 We have developed a new dataset of accumulation rates over the western interior of the Greenland ice sheet  
656 spanning the past 20 – 60 years, based on sixteen 22 – 32 m long firn cores and 4436 km of *in situ* GPR  
657 accumulation data. This accumulation record is internally consistent across the dataset and is validated by  
658 previous *in situ* field measurements and other radar-derived accumulation measurements (e.g Lewis et al.,  
659 2017).

660  
661 Overall, the Polar MM5 (Burgess et al., 2010), MAR (Fettweis et al., 2016), Box13 (Box et al., 2013), and  
662 RACMO2 (Noël et al., 2018) Regional Climate Models accurately capture large spatial patterns in  
663 accumulation rates over the GrIS, but show statistically significant differences from GPR accumulation rates  
664 on a regional basis. The average RMS difference between each model and GreenTrACS accumulation rates  
665 is  $0.068 \pm 0.065$  (MAR),  $0.048 \pm 0.045$  (Polar MM5),  $0.082 \pm 0.070$  (Box13),  $0.056 \pm 0.055$  (RACMO2),  
666 and  $0.045 \pm 0.045$  m w.e.  $a^{-1}$  (Bales09). These differences are on the same order as the uncertainties in the  
667 GreenTrACS and RCM accumulation rate estimates. While these average differences are small, we find  
668 differences of 0.1 to 0.4 m w.e.  $a^{-1}$  when we investigate at a local scale for each model.

669

670 While global climate models predict a 21<sup>st</sup>-century increase in precipitation over the GrIS (e.g. Bintanja and  
671 Selten, 2014), we observe a decrease in precipitation across the Western GrIS from 1996 – 2016 using records  
672 from firn cores, GPR, and published RCMs. We believe this study is the first to identify widespread negative  
673 GrIS precipitation trends during this period of enhanced surface melt, evident in these RCMs and our field  
674 observations (Graeter et al., 2018).

675

676 We attribute the decrease in accumulation rates over the Western GrIS between 1996 and 2016 to more  
677 persistently positive Greenland blocking in the summer. We find a statistically significant 25% reduction in  
678 the number of summer storms that precipitate over the GreenTrACS region since 1996. While warming  
679 temperatures from anthropogenic forcing and enhanced summer blocking have increased melt across the  
680 western percolation zone, here we show that summer blocking has also contributed to declining precipitation  
681 over the past two decades. This has led to a strongly negative SMB trend on both the input and output sides  
682 of the SMB equation that may not be accurately captured in global climate models that are currently unable  
683 to reproduce the recent increase in blocking. This highlights the importance of improving GCM projections  
684 of future summer blocking to accurately forecast Greenland precipitation and melt rates under stronger  
685 greenhouse gas forcing.

686

## 687 **5. Acknowledgements**

688 This project was supported by the US National Science Foundation (NSF) under grants DGE-1313911 and  
689 ARC-1417640. We would like to thank Mary Albert for providing field validation measurements, as well as  
690 Jason Box, Xavier Fettweis, and Brice Noel for providing the most recent Box13, MAR, and RACMO  
691 regional climate model outputs. Our successful data collection would not have been possible without the  
692 support of Ch2M Hill Polar Field Services, Kangerlussuaq International Science Support, and the Air  
693 National Guard 109<sup>th</sup> Airlift Wing. We thank the U.S. Ice Drilling Program for support activities through  
694 NSF Cooperative Agreement 1836328. Special thanks to Sean Birkel and the Danish Meteorological Institute  
695 for location-specific weather forecasts in Greenland. The authors would like to thank two anonymous  
696 reviewers for greatly improving the manuscript.

697

## 698 **6. Works cited**

699 Auger, J. D., Birkel, S. D., Maasch, K. A., Mayewski, P. A. and Schuenemann, K. C.: Examination of  
700 precipitation variability in southern Greenland, *J. Geophys. Res.*, 122(12), 6202–6216,

701 doi:10.1002/2016JD026377, 2017.

702 Bales, R. C., Guo, Q., Shen, D., McConnell, J. R., Du, G., Burkhart, J. F., Spikes, V. B., Hanna, E. and  
703 Cappelen, J.: Annual accumulation for Greenland updated using ice core data developed during 2000-2006  
704 and analysis of daily coastal meteorological data, *J. Geophys. Res. Atmos.*, 114(6), D06116,  
705 doi:10.1029/2008JD011208, 2009.

706 Ballinger, T. J., Hanna, E., Hall, R. J., Cropper, T. E., Miller, J., Ribergaard, M. H., Overland, J. E. and  
707 Høyer, J. L.: Anomalous blocking over Greenland preceded the 2013 extreme early melt of local sea ice,  
708 *Ann. Glaciol.*, 2013(March 2013), 1–10, doi:10.1017/aog.2017.30, 2017.

709 Benson, C. S.: Stratigraphic studies in the snow and firn of the Greenland Ice Sheet, *Folia Geogr. Danica*, 9,  
710 13–37, 1962.

711 Bevington, P. R. and Robinson, D. K.: *Data Reduction and Error Analysis for the Physical Sciences*, 2nd  
712 Editio., McGraw-Hill., 1992.

713 Bintanja, R. and Selten, F. M.: Future increases in Arctic precipitation linked to local evaporation and sea-  
714 ice retreat, *Nature*, 509(7501), 479–482, doi:10.1038/nature13259, 2014.

715 Box, J. E., Bromwich, D. H., Veenhuis, B. a., Bai, L. S., Stroeve, J. C., Rogers, J. C., Steffen, K., Haran, T.  
716 and Wang, S. H.: Greenland Ice Sheet Surface Mass Balance Variability ( 1988 – 2004 ) from Calibrated  
717 Polar MM5 Output \*, *J. Clim.*, 19(12), 2783–2801, doi:doi.org/10.1175/JCLI3738.1, 2006.

718 Box, J. E., Cressie, N., Bromwich, D. H., Jung, J. H., van den Broeke, M. R., van Angelen, J. H., Forster, R.  
719 R., Miège, C., Mosley-Thompson, E., Vinther, B. and McConnell, J. R.: Greenland ice sheet mass balance  
720 reconstruction. Part I: Net snow accumulation (1600-2009), *J. Clim.*, 26(11), 3919–3934, doi:10.1175/JCLI-  
721 D-12-00373.1, 2013.

722 van den Broeke, M. R., Bamber, J. L., Ettema, J., Rignot, E. J., Schrama, E., van de Berg, W. J., van  
723 Meijgaard, E., Velicogna, I. and Wouters, B.: Partitioning recent Greenland mass loss., *Science*, 326(5955),  
724 984–6, doi:10.1126/science.1178176, 2009.

725 van den Broeke, M. R., Enderlin, E. M., Howat, I. M., Kuipers Munneke, P., Noël, B., van de Berg, W. J.,  
726 van Meijgaard, E. and Wouters, B.: On the recent contribution of the Greenland ice sheet to sea level change,  
727 *Cryosph. Discuss.*, 1–26, doi:10.5194/tc-2016-123, 2016.

728 Brown, J., Harper, J., Pfeffer, W. T., Humphrey, N. and Bradford, J.: High-resolution study of layering within  
729 the percolation and soaked facies of the Greenland ice sheet, *Ann. Glaciol.*, 52(59), 35–42,  
730 doi:10.3189/172756411799096286, 2011.

731 Brown, J., Bradford, J., Harper, J., Pfeffer, W. T., Humphrey, N. and Mosley-Thompson, E.: Georadar-  
732 derived estimates of firn density in the percolation zone, western Greenland ice sheet, *J. Geophys. Res. Earth*  
733 *Surf.*, 117(1), 1–14, doi:10.1029/2011JF002089, 2012.

734 Buchardt, S. L., Clausen, H. B., Vinther, B. M. and Dahl-Jensen, D.: Investigating the past and recent  $\delta^{18}O$ -  
735 accumulation relationship seen in Greenland ice cores, *Clim. Past*, 8(6), 2053–2059, doi:10.5194/cp-8-2053-  
736 2012, 2012.

737 Burgess, E. W., Forster, R. R., Box, J. E., Mosley-Thompson, E., Bromwich, D. H., Bales, R. C. and Smith,  
738 L. C.: A spatially calibrated model of annual accumulation rate on the Greenland Ice Sheet (1958-2007), *J.*  
739 *Geophys. Res. Earth Surf.*, 115(2), 1–14, doi:10.1029/2009JF001293, 2010.

740 Enderlin, E. M., Howat, I. M., Jeong, S., Noh, M. J., Van Angelen, J. H. and Van Den Broeke, M. R.: An  
741 improved mass budget for the Greenland ice sheet, *Geophys. Res. Lett.*, 41(3), 866–872,  
742 doi:10.1002/2013GL059010, 2014.

743 Fettweis, X., Box, J. E., Agosta, C., Amory, C., Kittel, C. and Gallée, H.: Reconstructions of the 1900-2015

- 744 Greenland ice sheet surface mass balance using the regional climate MAR model, *Cryosph. Discuss.*,  
745 (November), 1–32, doi:10.5194/tc-2016-268, 2016.
- 746 Gerlitz, K., Knoll, M., Cross, G., Luzitano, R. and Knight, R.: Processing Ground Penetrating Radar Data to  
747 Improve Resolution of Near-Surface Targets, in *Symposium on the Application of Geophysics to*  
748 *Engineering and Environmental Problems 1993*, pp. 561–574, Environment and Engineering Geophysical  
749 Society., 1993.
- 750 Graeter, K. A., Osterberg, E. C., Ferris, D., Hawley, R. L., Marshall, H. P. and Lewis, G.: Ice Core Records  
751 of West Greenland Surface Melt and Climate Forcing, *Geophys. Res. Lett.*, doi:10.1002/2017GL076641,  
752 2018.
- 753 Hall, D. K., Comiso, J. C., DiGirolamo, N. E., Shuman, C. A., Key, J. R. and Koenig, L. S.: A satellite-  
754 derived climate-quality data record of the clear-sky surface temperature of the Greenland ice sheet, *J. Clim.*,  
755 25(14), 4785–4798, 2012.
- 756 Hall, D. K., Comiso, J. C., DiGirolamo, N. E., Shuman, C. A., Box, J. E. and Koenig, L. S.: Variability in  
757 the surface temperature and melt extent of the Greenland ice sheet from MODIS, *Geophys. Res. Lett.*, 40(10),  
758 2114–2120, doi:10.1002/grl.50240, 2013.
- 759 Hanna, E., Mernild, S. H., Cappelen, J. and Steffen, K.: Recent warming in Greenland in a long-term  
760 instrumental (1881–2012) climatic context: I. Evaluation of surface air temperature records, *Environ. Res.*  
761 *Lett.*, 7(4), 045404, doi:10.1088/1748-9326/7/4/045404, 2012.
- 762 Hanna, E., Jones, J. M., Cappelen, J., Mernild, S. H., Wood, L., Steffen, K. and Huybrechts, P.: The influence  
763 of North Atlantic atmospheric and oceanic forcing effects on 1900-2010 Greenland summer climate and ice  
764 melt/runoff, *Int. J. Climatol.*, 33(4), 862–880, doi:10.1002/joc.3475, 2013.
- 765 Hanna, E., Cropper, T. E., Hall, R. J. and Cappelen, J.: Greenland Blocking Index 1851-2015: a regional  
766 climate change signal, *Int. J. Climatol.*, 36(15), 4847–4861, doi:10.1002/joc.4673, 2016.
- 767 Hanna, E., Fettweis, X. and Hall, R. J.: Recent changes in summer Greenland blocking captured by none of  
768 the CMIP5 models, *Cryosph. Discuss.*, 1–8, doi:10.5194/tc-2018-91, 2018.
- 769 Harper, J., Humphrey, N., Pfeffer, W. T., Brown, J. and Fettweis, X.: Greenland ice-sheet contribution to  
770 sea-level rise buffered by meltwater storage in firn, *Nature*, 491(7423), 240–243, doi:10.1038/nature11566,  
771 2012.
- 772 Hawley, R. L., Courville, Z. R., Kehrl, L. M., Lutz, E. R., Osterberg, E. C., Overly, T. B. and Wong, G. J.:  
773 Recent accumulation variability in northwest Greenland from ground-penetrating radar and shallow cores  
774 along the Greenland Inland Traverse, *J. Glaciol.*, 60(220), 375–382, doi:10.3189/2014JoG13J141, 2014.
- 775 Herron, M. M. and Langway, C. C.: Firn densification: an empirical model., *J. Glaciol.*, 25(93), 373–385,  
776 doi:10.3198/1980JoG25-93-373-385, 1980.
- 777 Hofer, S., Bamber, J., Tedstone, A. and Fettweis, X.: Decreasing clouds drive mass loss on the Greenland  
778 Ice Sheet, *EGU Gen. Assem. Conf. Abstr.*, 19(6), 5086, 2017.
- 779 Karlöf, L., Isaksson, E., Winther, J. G., Gundestrup, N. S., Meijer, H. A. J., Mulvaney, R., Pourchet, M.,  
780 Hofstede, C., Lappégard, G., Petterson, R., van den Broeke, M. R. and Van De Wal, R. S. W.: Accumulation  
781 variability over a small area in east Dronning Maud Land, Antarctic, as determined from shallow firn cores  
782 and snow pits: Some implications for ice-core records, *J. Glaciol.*, 51(174), 343–352,  
783 doi:10.3189/172756505781829232, 2005.
- 784 Kobayashi, S., Ota, Y., Harada, Y., Ebita, A., Moriya, M., Onoda, H., Onogi, K., Kamahori, H., Kobayashi,  
785 C., Endo, H., Miyaoka, K. and Takahashi, K.: The JRA-55 Reanalysis: General Specifications and Basic  
786 Characteristics, *J. Meteorol. Soc. Japan. Ser. II*, 93(1), 5–48, doi:10.2151/jmsj.2015-001, 2015.

787 Koenig, L. S., Ivanoff, A., Alexander, P. M., MacGregor, J. A., Fettweis, X., Panzer, B., Paden, J. D., Forster,  
788 R. R., Das, I., McConnell, J. R., Tedesco, M., Leuschen, C. and Gogineni, S. P.: Annual Greenland  
789 accumulation rates (2009–2012) from airborne snow radar, *Cryosph.*, 10(4), 1739–1752, doi:10.5194/tc-10-  
790 1739-2016, 2016.

791 Kovacs, A., Gow, A. J. and Morey, R. M.: The in-situ dielectric constant of polar firn revisited, *Cold Reg.*  
792 *Sci. Technol.*, 23(3), 245–256, doi:10.1016/0165-232X(94)00016-Q, 1995.

793 De La Peña, S., Howat, I. M., Nienow, P. W., Van Den Broeke, M. R., Mosley-Thompson, E., Price, S. F.,  
794 Mair, D., Noël, B. and Sole, A. J.: Changes in the firn structure of the western Greenland Ice Sheet caused  
795 by recent warming, *Cryosphere*, 9(3), 1203–1211, doi:10.5194/tc-9-1203-2015, 2015.

796 Lavielle, M.: Using penalized contrasts for the change-point problem, *Signal Processing*, 85(8), 1501–1510,  
797 doi:10.1016/j.sigpro.2005.01.012, 2005.

798 Lewis, G., Osterberg, E. C., Hawley, R. L., Whitmore, B., Marshall, H. P. and Box, J. E.: Regional Greenland  
799 accumulation variability from Operation IceBridge airborne accumulation radar, *Cryosph.*, 11(2), 773–788,  
800 doi:10.5194/tc-11-773-2017, 2017.

801 McLeod, J. T. and Mote, T. L.: Linking interannual variability in extreme Greenland blocking episodes to  
802 the recent increase in summer melting across the Greenland ice sheet, *Int. J. Climatol.*, 36(3), 1484–1499,  
803 doi:10.1002/joc.4440, 2016.

804 Medley, B., Joughin, I., Das, S. B., Steig, E. J., Conway, H., Gogineni, S. P., Criscitiello, a. S., McConnell,  
805 J. R., Smith, B. E., van den Broeke, M. R., Lenaerts, J. T. M., Bromwich, D. H. and Nicolas, J. P.: Airborne-  
806 radar and ice-core observations of annual snow accumulation over Thwaites Glacier, West Antarctica  
807 confirm the spatiotemporal variability of global and regional atmospheric models, *Geophys. Res. Lett.*,  
808 40(14), 3649–3654, doi:10.1002/grl.50706, 2013.

809 Mernild, S. H., Hanna, E., McConnell, J. R., Sigl, M., Beckerman, A. P., Yde, J. C., Cappelen, J., Malmros,  
810 J. K. and Steffen, K.: Greenland precipitation trends in a long-term instrumental climate context (1890-2012):  
811 Evaluation of coastal and ice core records, *Int. J. Climatol.*, doi:10.1002/joc.3986, 2014.

812 Meyer, C. R. and Hewitt, I. J.: A continuum model for meltwater flow through compacting snow, *Cryosphere*,  
813 11(6), 2799–2813, doi:10.5194/tc-11-2799-2017, 2017.

814 Morlighem, M., Rignot, E. J., Mouginot, J., Seroussi, H. and Larour, E.: Deeply incised submarine glacial  
815 valleys beneath the Greenland ice sheet, *Nat. Geosci.*, 7(6), 18–22, doi:10.1038/ngeo2167, 2014.

816 Morris, E. M. and Wingham, D. J.: Densification of polar snow: Measurements, modeling, and implications  
817 for altimetry, *J. Geophys. Res. Earth Surf.*, 119(2), 349–365, doi:10.1002/2013JF002898, 2014.

818 Mosley-Thompson, E., McConnell, J. R., Bales, R. C., Li, Z., Lin, P.-N., Steffen, K., Thompson, L. G.,  
819 Edwards, R. and Bathke, D.: Local to regional-scale variability of annual net accumulation on the Greenland  
820 ice sheet from PARCA cores, *J. Geophys. Res.*, 106(D24), 33839, doi:10.1029/2001JD900067, 2001.

821 Mouginot, J., Rignot, E., Bjørk, A. A., van den Broeke, M., Millan, R., Morlighem, M., Noël, B., Scheuchl,  
822 B. and Wood, M.: Forty-six years of Greenland Ice Sheet mass balance from 1972 to 2018, *Proc. Natl. Acad.*  
823 *Sci.*, 201904242, doi:10.1073/pnas.1904242116, 2019.

824 Nghiem, S. V., Steffen, K., Neumann, G. and Huf, R.: Mapping of ice layer extent and snow accumulation  
825 in the percolation zone of the Greenland ice sheet, *J. Geophys. Res. Earth Surf.*, 110(2), 1–13,  
826 doi:10.1029/2004JF000234, 2005.

827 Nghiem, S. V., Hall, D. K., Mote, T. L., Tedesco, M., Albert, M. R., Keegan, K. M., Shuman, C. A.,  
828 DiGirolamo, N. E. and Neumann, G.: The extreme melt across the Greenland ice sheet in 2012, *Geophys.*  
829 *Res. Lett.*, 39(20), 6–11, doi:10.1029/2012GL053611, 2012.

830 Noël, B., van de Berg, W. J., Van Wessem, J. M., Van Meijgaard, E., Van As, D., Lenaerts, J. T. M.,  
831 Lhermitte, S., Munneke, P. K., Smeets, C. J. P. P., Van Ulft, L. H., Van De Wal, R. S. W. and Van Den  
832 Broeke, M. R.: Modelling the climate and surface mass balance of polar ice sheets using RACMO2 - Part 1:  
833 Greenland (1958-2016), *Cryosphere*, 12(3), 811–831, doi:10.5194/tc-12-811-2018, 2018.

834 Nye, J. F.: Correction factor for accumulation measured by the thickness of the annual layers in an ice sheet,  
835 *J. Glaciol.*, 4(36), 785–788, 1963.

836 Osterberg, E. C., Handley, M. J., Sneed, S. B., Mayewski, P. A. and Kreutz, K. J.: Continuous ice core melter  
837 system with discrete sampling for major ion, trace element, and stable isotope analyses, *Environ. Sci.*  
838 *Technol.*, 40(10), 3355–3361, doi:10.1021/es052536w, 2006.

839 Osterberg, E. C., Hawley, R. L., Wong, G. J., Kopec, B., Ferris, D. and Howley, J.: Coastal ice-core record  
840 of recent northwest Greenland temperature and sea-ice concentration, *J. Glaciol.*, 61(230), 1137–1146,  
841 doi:10.3189/2015JoG15J054, 2015.

842 Overly, T. B., Hawley, R. L., Helm, V., Morris, E. M. and Chaudhary, R. N.: Greenland annual accumulation  
843 along the EGIG line, 1959–2004, from ASIRAS airborne radar and neutron-probe density measurements,  
844 *Cryosph.*, 10(4), 1679–1694, doi:10.5194/tc-10-1679-2016, 2016.

845 Rennermalm, A. K., Moustafa, S. E., Mioduszewski, J., Chu, V. W., Forster, R. R., Hagedorn, B., Harper, J.  
846 T., Mote, T. L., Robinson, D. A., Shuman, C. A., Smith, L. C. and Tedesco, M.: Understanding Greenland  
847 ice sheet hydrology using an integrated multi-scale approach, *Environ. Res. Lett.*, 8(1), 015017,  
848 doi:10.1088/1748-9326/8/1/015017, 2013.

849 Rodriguez-Morales, F., Gogineni, S. P., Leuschen, C. J., Paden, J. D., Li, J., Lewis, C. C., Panzer, B., Gomez-  
850 Garcia Alvestegui, D., Patel, A., Byers, K., Crowe, R., Player, K., Hale, R. D., Arnold, E. J., Smith, L.,  
851 Gifford, C. M., Braaten, D. and Panton, C.: Advanced multifrequency radar instrumentation for polar  
852 Research, *IEEE Trans. Geosci. Remote Sens.*, 52(5), 2824–2842, doi:10.1109/TGRS.2013.2266415, 2014.

853 Sasgen, I., van den Broeke, M. R., Bamber, J. L., Rignot, E. J., Sorensen, L. S., Wouters, B., Martinec, Z.,  
854 Velicogna, I. and Simonsen, S. B.: Timing and origin of recent regional ice-mass loss in Greenland, *Earth*  
855 *Planet. Sci. Lett.*, 333–334, 293–303, doi:10.1016/j.epsl.2012.03.033, 2012.

856 Selesnick, I. W. and Sidney Burrus, C.: Generalized digital butterworth filter design, *IEEE Trans. Signal*  
857 *Process.*, 46(6), 1688–1694, doi:10.1109/78.678493, 1998.

858 Serreze, M.: Northern Hemisphere cyclone locations and characteristics from NCEP/NCAR reanalysis data,  
859 Verison 1, Natl. Snow Ice Data Center, Boulder, CO, Digit. media.[Available online <http://nsidc.org/data/nsidc-0423.html>], 2009.

861 Spikes, V. B., Hamilton, G. S., Arcone, S. A., Kaspari, S. and Mayewski, P. A.: Variability in accumulation  
862 rates from GPR profiling on the West Antarctic plateau, *Ann. Glaciol.*, 39, 238–244,  
863 doi:10.3189/172756404781814393, 2004.

864 Trusel, L. D., Das, S. B., Osman, M. B., Evans, M. J., Smith, B. E., Fettweis, X., McConnell, J. R., Noël, B.  
865 and van den Broeke, M. R.: Nonlinear rise in Greenland runoff in response to post-industrial Arctic warming,  
866 *Nature*, 564(7734), 104–108, doi:10.1038/s41586-018-0752-4, 2018.

867 Vandecrux, B., Fausto, R. S., Langen, P. L., Van As, D., MacFerrin, M., Colgan, W., Ingeman-Nielsen, T.,  
868 Steffen, K., Jensen, N. S., Møller, M. T. and Box, J. E.: Drivers of Firn Density on the Greenland Ice Sheet  
869 Revealed by Weather Station Observations and Modelling, *J. Geophys. Res. Earth Surf.*,  
870 doi:10.1029/2017JF004597, 2018.

871 Vernon, C. L., Bamber, J. L., Box, J. E., Van Den Broeke, M. R., Fettweis, X., Hanna, E. and Huybrechts,  
872 P.: Surface mass balance model intercomparison for the Greenland ice sheet, *Cryosph.*, 7(5), 599–614,  
873 doi:10.5194/tc-7-599-2013, 2013.

- 874 Wong, G. J., Hawley, R. L., Lutz, E. R. and Osterberg, E. C.: Trace-element and physical response to melt  
875 percolation in Summit (Greenland) snow, *Ann. Glaciol.*, 54(63), 52–62, doi:10.3189/2013aog63a602, 2013.
- 876 Wong, G. J., Osterberg, E. C., Hawley, R. L., Courville, Z. R., Ferris, D. G. and Howley, J.: Coast-to-interior  
877 gradient in recent northwest Greenland precipitation trends (1952 – 2012 ), *Environ. Res. Lett.*, 10(11),  
878 114008, doi:10.1088/1748-9326/10/11/114008, 2015.
- 879 Yilmaz, Ö.: *Seismic Data Analysis*, Society of Exploration Geophysicists., 2001.
- 880 Zumberge, J. F., Heflin, M. B., Jefferson, D. C., Watkins, M. M. and Webb, F. H.: Precise point positioning  
881 for the efficient and robust analysis of GPS data from large networks, *J. Geophys. Res. Solid Earth*, 102(B3),  
882 5005–5017, doi:10.1029/96JB03860, 1997.
- 883